Sensitivity of ice accretion and aerodynamic performance degradation to critical physical and modeling parameters affecting airfoil icing

L. Prince Raj*, K. Yee[†], and R. S. Myong[‡]

*Department of Aerospace Engineering and Applied Mechanics, Indian Institute of Engineering Science & Technology, Shibpur, Howrah 711103, India

[†]Department of Mechanical and Aerospace Engineering, Seoul National University, Seoul 08826, South Korea

[‡] School of Mechanical and Aerospace Engineering and Research Center for Aircraft Core Technology, Gyeongsang National University, Jinju, Gyeongnam 52828, South Korea

myong@gnu.ac.kr

Abstract

Understanding ice accretion and aerodynamic performance degradation is essential in any aircraft certification program to ensure safe flight in icing conditions. In addition to well-known meteorological icing parameters and flight conditions, several physical and modeling parameters are known to play a critical role in the process of ice accretion on aircraft surfaces. In this study, the sensitivity of eight ice shape attributes and ice mass to five critical physical and modeling parameters was investigated using a high-fidelity computational method. In the sensitivity analysis, the Sobol sequence sampling method, the radial basis function, and Sobol's method were used to generate the sampling points in the given design space, to construct the metamodel, and evaluate the sensitivity indices, respectively. Based on the sensitivity indices, the number of shots turned out to be the largest contributor in the sum of both the first-order and total effects. Surface roughness was also shown to be the dominant parameter affecting the ice horn height and ice horn position because of the strong connection between roughness and heat flux. In general, it was shown that to varying degrees each parameter has a direct effect on ice accretion attributes and aerodynamic performance degradation. Further, it was noted that the parameters' interactions have a significant effect on the ice accretion attributes.

1. Introduction

Ice accretion on aircraft flying through icing clouds is a severe safety hazard to aircraft operations[1, 2]. Along with other safety related certifications, icing certification to ensure safe flight in icing conditions is required before operation. There are several engineering methods available for use in aircraft icing design and certification processes, including analysis [3, 4] and computational fluid dynamics (CFD) [5, 6], tunnel testing (dry and icing wind tunnels) [7-11], flight testing (artificial ice shapes, icing tanker, and natural icing) [12-14], and similarity argument for derivatives of an aircraft.

Wind tunnel icing testing can generate the ice shapes that accrete on the surfaces of model aircraft under icing conditions, and is the only method for testing running-wet ice protection systems (IPS) for design cases [15-17]. The ice shapes obtained from icing wind tunnel testing can be manufactured and then attached to aircraft components to evaluate how they degrade aerodynamic performance during flight testing. However, wind tunnel icing testing suffers from the very complicated scaling laws needed to determine collection efficiencies for water droplets and ice shapes, and therefore it cannot handle all the meteorological icing conditions prescribed by an icing certification envelope. Hence, the computational method—the only method capable of exploring the full icing envelope—has been increasingly employed to predict ice accretion shapes [18-20], for the design of ice protection systems [21, 22], and to estimate the aerodynamic performance degradation of aircraft due to icing [20, 23, 24].

Figure 1 highlights the *physical and modeling parameters* that are critically involved in the ice accretion process on aircraft surfaces, including the well-known meteorological icing parameters (liquid water content (LWC), mean volumetric diameter (MVD), temperature) and flight conditions (velocity, altitude, exposure time). Among five physical and modeling parameters, surface roughness is considered the most prominent parameter affecting the physics of ice accretion. Changes in surface roughness are known to significantly change the location, mass, and shape of accreted ice [25]. Other physical and modeling parameters, such as ice density, evaporation, droplet distribution, and the number of shots of computational simulations are also known to play a critical role in the simulation of ice accretion on

aircraft surfaces. Hence, a careful assessment of these physical and modeling parameters is essential to gain a deeper understanding of ice accretion, and to accurately predict ice shape, mass, and any degradation of aerodynamic performance. Poor understanding of the physical and modeling parameters introduced in the model can not only lead to an incorrect assessment of the validity of the physical model and the associated CFD method but can also result in errors from inaccuracies calibrated into the supposedly accurate physical model.

In general, ice accretion is strongly influenced by shear stress, heat flux, and the droplet collection efficiency of a surface [20, 26, 27]. Shear stress and heat flux are in turn heavily affected by surface roughness. Hence, in the modeling of ice accretion, a careful assessment of surface roughness is necessary [28]. However, because of the theoretical and computational complexities involved, most of current ice accretion solvers use empirical correlations [29, 30], which are tailored in terms of the free stream velocity, LWC, MVD, the surface temperature, and the chord length of the wing. These empirical correlations are questionable, since they were derived from wind tunnel tests conducted under Reynolds numbers that are substantially lower than actual in-flight Reynolds numbers. In addition, the surfaces of the wind tunnel test models need in principle to be properly machined to replicate the roughness of a real aircraft surface, but this has not been the case in most previous wind tunnel testing.

Ice density information is required to determine the accreted ice mass and ice thickness on a surface. However, in the physical process of modeling ice accretion, ice density is arbitrarily selected from a range of 400 to 917 kg/m^3 or is chosen based on empirical relations [31, 32]. There is presently no rule of thumb for selecting ice density, and no convincing rationale for using empirical equations which are basically derived from very limited icing conditions. Also, because of the water vapor concentration gradient, a fraction of the liquid water on the surface will evaporate into the air, changing the amount of ice accumulation in ice accretion models. As a result, the formulas used to model the water vapor gradient and evaporation mass may affect ice accretion as well.
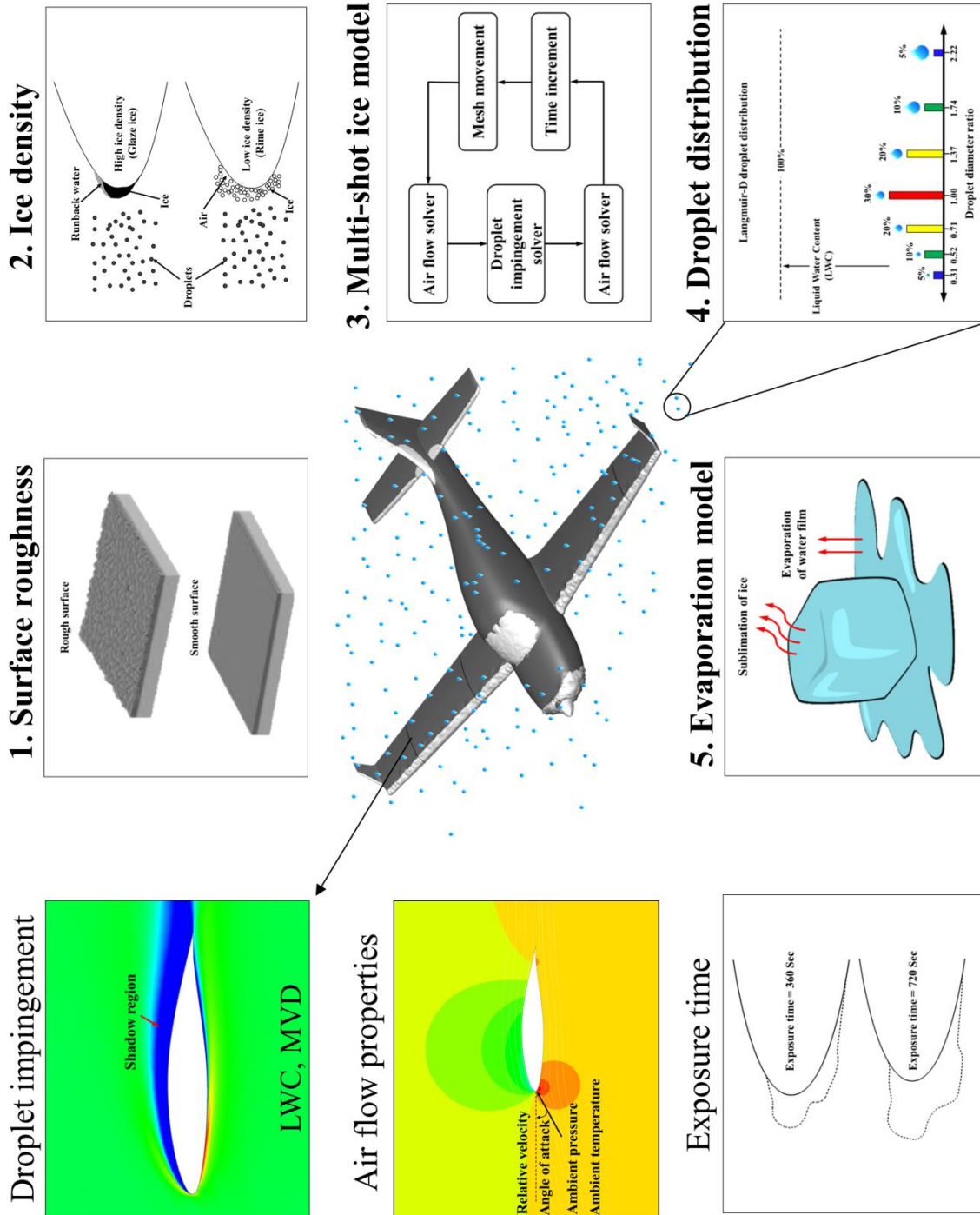
2. Ice density

3. Multi-shot ice model

4. Droplet distribution

1. Surface roughness

5. Evaporation model

Droplet impingement

LWC, MVD

Air flow properties

Exposure time

Fig. 1. Five critical physical and modeling parameters affecting ice accretion shape and mass**.**

Different distributions of droplets may also affect droplet collection efficiency and subsequent ice accumulation. Mono-disperse droplet distribution is widely used to simulate droplet impingements in order to reduce computational cost, even though natural droplet conditions in icing clouds follow a poly-disperse droplet distribution, for instance, the Langmuir-D droplet distribution, with seven bins, illustrated in Fig. 1.

Another critical modeling parameter in ice accretion is the treatment of the air flow field and ice accumulation with respect to time. As highlighted in Fig. 2, in the conventional (less time-consuming) single-shot approach, the ice shape is computed based solely on the initial (one-time) air flow field and droplet solution. On the other hand, in the accurate (but more time-consuming) multi-shot approach, the air flow field and droplet solutions are updated after a certain number of ice accretion time steps and automatic grid regenerations.
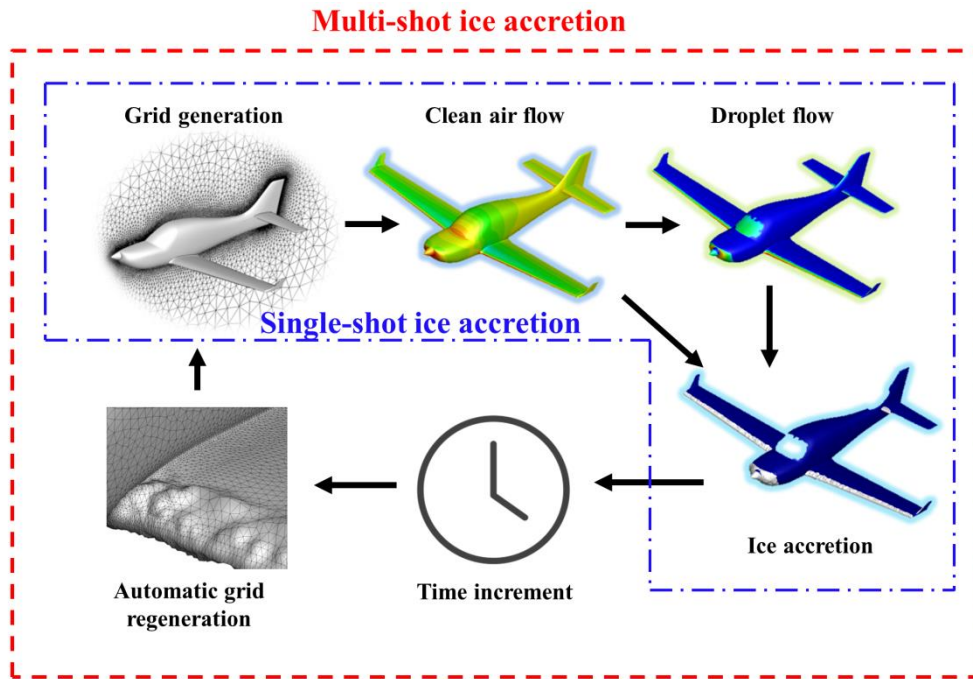

Fig. 2. Illustration of single shot and multi-shot ice accretion approach.

Miller *et al.* [25] in 2005 experimentally investigated the effects of meteorological parameters (LWC, MVD, and temperature) on ice shape. The experiments were performed on a NACA0012 airfoil in the Icing Research Tunnel (IRT) at the NASA Glenn Research Center. The observations demonstrated that

the ice horn angle and mass were sensitive to variations in the meteorological parameters. Further, using experimental data from Miller *et al.*, Campbell [33] investigated the sensitivity of airfoil aerodynamic performance degradation to meteorological parameters. They evaluated the effects of meteorological parameters on ice accretion geometry, which is defined in terms of normalized horn height, ice horn angle, normalized horn position, normalized icing limit, and ice mass, as illustrated in Fig. 3.
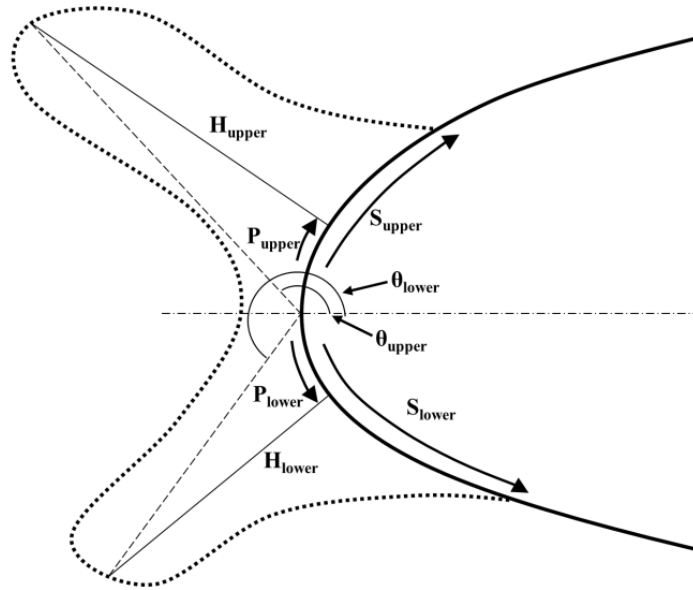

Fig. 3. Ice geometry attributes involved in the evaluation of the critical effects of the physical and modeling parameters.

Wright *et al.* [34, 35] used different Navier-Stokes-Fourier codes along with LEWICE to validate the ice shapes and aerodynamic degradations. The simulated results were compared with the set of experimental results for various airfoils at different meteorological conditions. The investigation showed that the computed results are in acceptable accuracy for most cases. Son *et al.* [36, 37] computationally investigated the effects of meteorological parameters and flight conditions (LWC, droplet diameter, free stream velocity and temperature) on ice accretion. DeGennaro *et al.* [38] conducted uncertainty quantification for airfoil icing—quantifying the effects of ice shape uncertainty on the aerodynamic performance of an airfoil—using polynomial chaos expansions. A fast uncertainty quantification

prediction using polynomial chaos expansion was shown to match the results of Monte Carlo simulations well.

Many investigations on the aerodynamic degradation of iced airfoils have also been reported in the literature [18, 20, 23, 39-41]. For instance, Marongiu *et al.* [40] investigated the flow field over an NLF-0414 airfoil with a prescribed ice shape using three different flow solvers with two turbulence models. Recently, Chen *et al.* [41] investigated the aerodynamic characteristics of an iced rotor in forward flight.

The present study focuses on how sensitively critical *physical and modeling* parameters affect the modeling of ice accretion and aerodynamic performance degradation. Understanding ice accretion (ice shape and mass) and aerodynamic performance degradation is essential to any aircraft icing certification campaign. Even a few grams (exceeding 130 grams) of ice ingestion in an engine intake can jeopardize the whole icing certification effort. And physical parameters like surface roughness are known to be critically involved in the physical ice accretion process on aircraft surfaces.

For these reasons, there is a strong need to investigate the sensitivity of critical physical and modeling parameters beyond much-studied obvious meteorological parameters like LWC and MVD, or flight conditions like velocity. *The present study may be considered the first attempt to systematically investigate the sensitivity of ice accretion and aerodynamic performance degradation to critical physical and modeling parameters.*

In this study, the effects of various critical physical and modeling parameters on ice geometry were first investigated. For this purpose, in-house unified computational solvers for clean air, droplet impingement, ice accretion including rime and glaze ices, and the analysis of aerodynamic performance degradation were developed based on an unstructured upwind finite volume formulation. The effects of parameters on the ice shape attributes were then ranked by proper sensitivity indices. A sampling method based on the Sobol sequence was used to characterize the ice shape attributes, while radial basis function (RBF) metamodeling was used in modeling the impact of the icing parameters' uncertainty. The results were then fed into a variance-based global sensitivity analysis to rank the first-order and higher-order

interaction effects of icing physical and modeling parameters. Finally, the effects of primary physical (surface roughness and ice density) and modeling (multi-shot) parameters on aerodynamic performance degradation of an iced airfoil were investigated.

2. Mathematical and computational models for ice accretion simulation

The ice accretion simulation can be achieved by accurately modeling three physical processes: the aerodynamic flow, the water droplet impingement, and the thermodynamic ice accretion process. In atmospheric icing condition, the ratio of the mass of water droplets of small size (on the order of a few tens of micrometers in diameter) to the mass of air in unit volume is known to be in the range of 10^{-3}. In addition, the corresponding Stokes number—characterizing the behavior of particles suspended in a fluid flow—inside a cloud composed of air and small super-cooled droplets of liquid water is smaller than 0.1 in most flight conditions, the air-mixed droplet multiphase flow field can be solved using a weakly coupled (one-way coupling) algorithm [6, 27]. Hence, the effects of micro-size droplets on air flow can be ignored, and the air data is provided as a source term in the Eulerian droplet equations. Finally, the ice accretion can be predicted by a thermodynamic model using the solutions from the air and droplet solvers.

2.1. Air flow field

The well-known compressible Navier-Stokes-Fourier equations were employed as the clean air solver,

$$
\begin{bmatrix} \rho_g \\ \rho_g \mathbf{u}_g \\ \rho_g E \end{bmatrix}_t + \nabla \cdot \begin{bmatrix} \rho_g \mathbf{u}_g \\ \rho_g \mathbf{u}_g \mathbf{u}_g + p\boldsymbol{I} \\ (E+p)\mathbf{u}_g \end{bmatrix} = \nabla \cdot \begin{bmatrix} 0 \\ \boldsymbol{\tau} \\ \boldsymbol{\tau} \cdot \mathbf{u}_g + \mathbf{Q} \end{bmatrix},
\tag{1}
$$

where

$$
\boldsymbol{\tau} = 2\mu \big[\nabla \mathbf{u}_g \big]^{(2)}, \quad \mathbf{Q} = k\nabla T.
\tag{2}
$$

Here ρ_g, $\mathbf{u}_g$, p, and E represent the density, the velocity vector, the pressure, and the total energy of the air, respectively. The non-conserved variables $\boldsymbol{\tau}$ and $\mathbf{Q}$ denote the viscous shear stress tensor and the heat flux vector, respectively. In equation (2), the symbol $[\mathbf{A}]^{(2)}$ in the viscous shear stress tensor stands for the

traceless symmetric part of tensor **A**. μ and k are the viscosity and thermal conductivity, respectively, and depend on the air temperature. For air flow, the ideal equation of state $p = \rho_g RT$ is used.

2.2. Eulerian description of droplet flow

A shallow water droplet model based on the Eulerian framework developed in a previous work [42] was employed for the droplet solver. In the present weakly coupled algorithm, the Eulerian droplet solver is provided with the air flow information computed by the air flow solver through the source term. The formulation is based on splitting of the original Eulerian droplet system into the well-posed hyperbolic part and the source term, which circumvents the non-strictly hyperbolic nature of the droplet equations. Then it is again applied, as summarized below,

$$\begin{bmatrix} \rho \\ \rho\mathbf{u} \end{bmatrix}_t + \nabla \cdot \begin{bmatrix} \rho\mathbf{u} \\ \rho\mathbf{u}\mathbf{u} + \rho g d\mathbf{I} \end{bmatrix} = \begin{bmatrix} 0 \\ \mathbf{S}_D + \mathbf{S}_G + \mathbf{S}_S \end{bmatrix}. \tag{3}$$

Note that the equation of the droplet model (3) is a convection-type equation with no diffusion terms. Here ρ, $\mathbf{u}$, and d denote the density of droplets in terms of liquid water content (LWC), the velocity components of the droplet, and the reference size of droplets, respectively. $\mathbf{S}_D = A_u (\mathbf{u}_g - \mathbf{u})$ represents the drag on droplets caused by the airflow. $\mathbf{S}_G = \rho g[0, 0, 1\text{-}\rho_g/\rho_w]^T$, where g, ρ_g and ρ_w denote acceleration due to gravity, and the density of air and water, respectively, represents the resultant force of gravity and the buoyancy of the droplets. $\mathbf{S}_S = \nabla \cdot (\rho g d)\mathbf{I}$ is an added source term to circumvent the non-strictly hyperbolic nature of the droplet equations. The coefficient A_u can be expressed as,

$$A_u = 0.75 \cdot \rho \cdot C_{D_u} \cdot Re_u \cdot \mu / \rho_w \cdot MVD^2 , \quad Re_u = \rho_g \cdot MVD \cdot |\mathbf{u}_g - \mathbf{u}| / \mu. \tag{4}$$

Here μ and MVD are the dynamic viscosity of the gas and the mean volume diameter of the droplet, respectively. Re_u and C_{D_u} are the Reynolds number of the droplets and the drag coefficients of the spherical droplets, respectively. The drag coefficient can be obtained from Lapple [43] as follows,

$$C_{D_u} = \frac{24}{Re_u} \left(1 + 0.0197 Re_u^{0.63} + 2.6\text{e}^{-4} \cdot Re_u^{1.38}\right), \tag{5}$$

which is valid for $Re_u < 1000$.

2.3. Partial differential equation (PDE) based ice accretion model

The PDE based ice accretion model uses the air solution over the surface, and the droplet impingement distribution as input to predict ice accretion on a given surface. The ice accretion model solves a mass and energy balance along the surface to predict the amount of water accumulation $(\dot{m}_{ice})$ and equilibrium temperature (T_{equi}). The unfrozen water is considered as runback water, and the thickness of the water film on the surface (h_f) is evaluated. Once the mass of ice accretion is evaluated, other necessary outputs such as ice thickness and volume can be evaluated. Finally, the iced surface geometry is predicted based on the results of ice thickness. In ice accretion simulations, the film thickness is in the range of 10 µm [44]. Hence, by assuming velocity distribution within the film is linear, the velocity of the water film $(\bar{u}_f)$ can be represented as a function of the water film thickness and shear stress (τ_{wall}) as follows,

$$\bar{u}_f = f\left(h_f\right) = \frac{1}{h_f} \int_0^{h_f} u_f \, dh = \frac{h_f}{2\mu_w} \tau_{wall}. \tag{6}$$

The resulting PDE based thermodynamic model adopted from previous literatures [26, 45] can be written as,

$$\frac{\partial \mathbf{U}}{\partial t} + \nabla \cdot \mathbf{F}(\mathbf{U}) = \mathbf{S}, \tag{7}$$

where

$$\mathbf{U} = \begin{bmatrix} h_f \\ h_f T_{equi} \end{bmatrix}, \quad \mathbf{F}(\mathbf{U}) = \begin{bmatrix} \dfrac{h_f^2}{2\mu_w} \boldsymbol{\tau}_{wall} \\ \dfrac{h_f^2 T_{equi}}{2\mu_w} \boldsymbol{\tau}_{wall} \end{bmatrix}, \quad \mathbf{S} = \begin{bmatrix} \dfrac{S_M}{\rho_w} \\ \dfrac{S_E}{\rho_w Cp_w} + \dfrac{T_c S_M}{\rho_w} \end{bmatrix}, \tag{8}$$

$$S_M = U_\infty LWC_\infty \beta - \dot{m}_{evap} - \dot{m}_{ice},$$

$$S_E = \left[Cp_w \tilde{T}_{d,\infty} + \frac{\|u_d\|^2}{2} \right] \times U_\infty LWC_\infty \beta - L_{evap} \dot{m}_{evap} \qquad (9)$$

$$+ h_c \left(T_{equi} - T_\infty \right) + \sigma \varepsilon \left[T_{equi}^4 - T_\infty^4 \right] + \dot{m}_{ice} \left[L_{fus} - Cp_{ice} T_{equi} \right].$$

Here μ_w, Cp_w, Cp_{ice} represent the dynamic viscosity, the specific heat at constant pressure for water, and specific heat at constant pressure for ice, respectively. The instantaneous evaporation mass, latent heat of fusion, and latent heat of evaporation are represented by $\dot{m}_{evap}, L_{fus}$ and L_{evap}, respectively. Further, T_c,

$\tilde{T}_{d,\infty}$ and u_d represent the critical temperature (T_c = 273.15 K), droplet temperature in degree Celsius, and droplet impact velocity vector, respectively. The terms ε and σ represents the solid emissivity and Boltzmann constant (σ_a = 1.38064852 × 10^{-23} m^2 kg s^{-2} K^{-1}), respectively.

The clean air solver provides the wall shear stress (τ_{wall}) and heat transfer coefficient (h_c) as inputs to the ice accretion solver. The shallow water type droplet solver provides the droplet impact velocity and collection efficiency as inputs to the ice accretion solver. There are three unknowns to be computed: water film thickness, equilibrium temperature, and mass accumulation. Since there are only two governing equations available, compatibility relations are necessary to close the system. Based on physical behavior, the following compatibility equations can be derived,

$$h_f \geq 0, \dot{m}_{ice} \geq 0, h_f T_{equi} \geq h_f T_C, \dot{m}_{ice} T_{equi} \leq \dot{m}_{ice} T_C. \qquad (10)$$

The first compatibility relation ensures that the film thickness remains positive. The second compatibility relation prevents the melting of accreted ice. The third compatibility relation ensures that the water film only can exist at an equilibrium temperature above the freezing point. Finally, the fourth compatibility equation stipulates that ice cannot form for equilibrium temperatures above the freezing point.

By using these compatibility equations, each cell in the domain was explicitly solved individually with small time steps [18-20]. The governing equations together with the compatibility relations for the water film on the surface of the body were solved by a cell-centered a finite volume method. The computation

elements were spread over the surface of the body and need to be solved using some numerical technique. The Godunov-type Roe's approximate Riemann solver [46] was used to discretize the divergence terms in the governing equations.

2.4. Unified FVM framework for ice accretion modeling

In the present study, an unstructured mesh is used because of its flexibility in handling the complex ice shape geometries and local mesh refinement. In the unified framework of ice accretion modeling, the same mesh was used for all the solvers to minimize data loss between the solvers. In addition, the cell-centered finite volume method (FVM) was used to solve all the governing equations.

2.4.1. FVM numerical modeling of the air solver

The numerical scheme is based on a cell-centered finite volume method with the Roe's flux-difference splitting method [46]. The Roe's approximate solver can work in both a cell-centered and a dual control volume scheme framework. The flux across each face c of a control volume face can be expressed as,

$$\mathbf{F}_c = \frac{1}{2}\Big[\mathbf{F}(\mathbf{U}_L) + \mathbf{F}(\mathbf{U}_R) - \big|\overline{\mathbf{A}}_{Roe}\big|(\mathbf{U}_R - \mathbf{U}_L)\Big], \text{ where } \big|\overline{\mathbf{A}}_{Roe}\big| = \overline{\mathbf{R}}\overline{\mathbf{\Lambda}}\overline{\mathbf{L}}. \tag{11}$$

In equation (11) $\mathbf{U}_L$ and $\mathbf{U}_R$ are the dependent variables vectors evaluated at the left and right states of face c, respectively. $\mathbf{F}(\mathbf{U}_L)$ and $\mathbf{F}(\mathbf{U}_R)$ are the flux vectors evaluated using the dependent variable vectors of respective cells. Matrix $\overline{\mathbf{A}}_{Roe}$ can be constructed from the flux Jacobian with the right and left eigenvector matrices $\overline{\mathbf{L}}$, $\overline{\mathbf{R}}$ and a diagonal matrix with the absolute value of the eigenvalues $\overline{\mathbf{\Lambda}}$. In equation (11), the product of $\overline{\mathbf{A}}_{Roe}$ and the difference between the right and left states can be expressed as,

$$\big|\overline{\mathbf{A}}_{Roe}\big|(\mathbf{W}_R - \mathbf{W}_L) = \big|\Delta\mathbf{F}_1\big| + \big|\Delta\mathbf{F}_{1,2,3}\big| + \big|\Delta\mathbf{F}_5\big|. \tag{12}$$

Here, $\big|\Delta\mathbf{F}_1\big|$, $\big|\Delta\mathbf{F}_{1,2,3}\big|$, and $\big|\Delta\mathbf{F}_5\big|$ are the magnitude of the flux differences. By using Roe's averaging, the jump condition can be evaluated.

Next, the viscous flux is evaluated from the flow quantities and its first derivatives at the face of the control volume. The control volume was chosen to be the same in both the convective and viscous fluxes

to obtain a consistent spatial discretization. The viscous fluxes are elliptic in nature, which can be easily calculated by a simple average of the velocity components, heat conduction coefficient, and dynamic viscosity, at the face of the control volume. However, the gradient terms need special treatment to avoid the unbalanced weights due to the unstructured nature of the grid. Hence, a modified averaging [47] was used in the current simulation, which leads to strongly coupled stencils on unstructured grids.

Moreover, the governing equations for air solver were solved using the method of lines. An explicit multi-stage Runge-Kutta scheme [48] was employed for the time-dependent compressible Navier-Stokes-Fourier equations. In order to accelerate the steady-state solution, a local time stepping scheme was used,

$$\mathbf{U}_I^{n+1} = \mathbf{U}_I^{(m)} = \mathbf{U}_I^{(0)} - \alpha_i \frac{\Delta t_I}{\Omega_I} \mathbf{R}_I^{(i-1)}. \tag{13}$$

Here, α_i denotes the stage coefficients, $\mathbf{R}_I^i$ represents the residual evaluated with the solution $\mathbf{U}_I^n$ from the i-th stage. The time step Δt can be determined for a control volume Ω from the approximate relation,

$$\Delta t = \sigma \frac{\Omega}{\left(\Lambda_c + C\Lambda_v \right)}. \tag{14}$$

The Λ_c and Λ_v are the spectral radii of the convective and viscous fluxes, respectively. The constant C is usually set to be $1 \leq C \leq 4$ for cell-centered schemes and σ represents the CFL number.

2.4.2. FVM numerical modeling of droplet solver

The complete set of Eulerian droplet equations (3) with the source terms can be written as,

$$\frac{\partial}{\partial t} \int_\Omega \mathbf{U} d\Omega + \oint_{\partial\Omega} \mathbf{F} dS = \int_\Omega (\mathbf{S}_D + \mathbf{S}_G + \mathbf{S}_S) d\Omega. \tag{15}$$

They can be rewritten over the domain Ω as follows,

$$\frac{\partial \mathbf{U}}{\partial t} = -\frac{1}{\Omega} \left[\oint_{\partial\Omega} \mathbf{F} dS - \int_\Omega (\mathbf{S}_D + \mathbf{S}_G + \mathbf{S}_S) d\Omega \right]. \tag{16}$$

The surface integral on the right-hand side of equation (16) can be approximated using the sum of the fluxes crossing the faces of the control volume. In the finite volume method, it is assumed that the flux is

constant along the individual face of a cell and is evaluated at the midpoint of the face. The discretized form of the equation (16) can be written as,

$$\frac{d\mathbf{U}}{dt} = -\frac{1}{\Omega}\left[\sum_{k=1}^{N_f}\mathbf{F}_k\Delta S_k - (\mathbf{S}_D + \mathbf{S}_G)\Omega - gd\sum_{k=1}^{N_f}\rho_k\begin{pmatrix}0\\\mathbf{n}_k\end{pmatrix}\Delta S_k\right].$$

(17)

Note the volume integral of $\mathbf{S}_S$ is reduced to interface integrals, owing to its special form of $\nabla\cdot(\rho gd\mathbf{I})$. In equation (17), the flux was evaluated using the Harten-Lax-van Leer-contact (HLLC) approximation [42], and the source terms were determined using the information provided by the air solver. The temporal discretization is based on an explicit multi-stage Runge-Kutta scheme as described in equation (13). The time step Δt can be determined for a control volume Ω from the approximate relation,

$$\Delta t = \sigma\frac{\Omega}{\Lambda}, \text{ where } \Lambda = \sum_{i=1}^{N_f}\left(\left|\mathbf{v}_i\cdot\mathbf{n}_i\right| + c_i\right)\Delta S_i.$$

(18)

The CFL number and the coefficients for the five stages of the second-order upwind spatial discretization were followed as prescribed by the literature [47].

2.4.3. FVM numerical modeling of ice accretion solver

A Godunov-type Roe's approximate solver was used to discretize the governing equations of ice accretion. Equation (6) can be expressed as,

$$\frac{\partial}{\partial t}\int_\Omega \mathbf{U}d\Omega + \oint_{\partial\Omega}\mathbf{F}dS = \int_\Omega \mathbf{S}\,d\Omega.$$

(19)

The flux across each face of a control volume can be given as,

$$\mathbf{F}_C = \frac{1}{2}\left(\mathbf{F}(\mathbf{U}_L) + \mathbf{F}(\mathbf{U}_R)\right)\cdot\mathbf{n} - \frac{1}{2}\left|\mathbf{J}(\mathbf{U}_{L+1/2})\cdot\mathbf{n}\right|(\mathbf{U}_R - \mathbf{U}_L),$$

$$\mathbf{J}(\mathbf{U}_{L+1/2}) = \mathbf{J}\left(\frac{\mathbf{U}_L - \mathbf{U}_R}{2}\right).$$

(20)

The Jacobian matrix and eigenvalues of the system of equations can be written as, respectively,

14

$$\mathbf{J}(\mathbf{U}) \cdot \mathbf{n} = (\boldsymbol{\tau}_{wall} \cdot \mathbf{n}) \begin{bmatrix} \dfrac{h_f}{\mu_w} & 0 \\ \dfrac{h_f T_{equi}}{2\mu_w} & \dfrac{h_f}{2\mu_w} \end{bmatrix}, \tag{21}$$

$$\lambda_1 = \frac{h_f}{2\mu_w}\tau_{wall}, \quad \lambda_2 = \frac{h_f}{\mu_w}\tau_{wall}. \tag{22}$$

Finally, the cell i can be solved using the following equations

$$\Omega\left(\rho_w \frac{\partial h_i}{\partial t} - S_{M_i}\right) + \sum_{j=1}^{N_f} F_{ij}^M = 0,$$

$$\Omega\left(\rho_w c_{p,w} \frac{\partial h_i T_j}{\partial t} - S_{E_i}\right) + \sum_{j=1}^{N_f} F_{ij}^E = 0. \tag{23}$$

For convenience, h_f is specified as h, and T_{equi} is specified as T. In the system of equations, $\dot{m}_{ice}$ is also an

unknown property and the discretized equation can thus be written as,

$$\left[\rho_w \frac{h_i^{n+1} - h_i^n}{\Delta t} + \dot{m}_{ice}^{n+1} - S_{M_i}'\right]\Omega + \sum_{j=1}^{N_f} R_{ij}^M = 0,$$

$$\left[\rho_w Cp_w \frac{h_i^{n+1} T_i^{n+1} - h_i^n T_i^n}{\Delta t} - \dot{m}_{ice}^{n+1}\left(L_{fus}(T_c) - Cp_{ice}(T_i^{n+1} - T_c) - Cp_w T_c\right) - S_{E_i}'\right]\Omega \tag{24}$$

$$+ \sum_{j=1}^{N_f} R_{ij}^E = 0.$$

Here S_M' and S_E' are defined as the source terms of the mass and energy equations without the $\dot{m}_{ice}$ term,

$$S_{M_i}' = U_\infty LWC_\infty \beta - \dot{m}_{evap},$$

$$S_{E_i}' = U_\infty LWC_\infty \beta\left[Cp_w(T_{d,\infty} - T_c) + \frac{\|\mathbf{u}_d\|^2}{2}\right] - L_{evap}\dot{m}_{evap} + h_c(T_i^{n+1} - T_\infty) + \tag{25}$$

$$\sigma\varepsilon\left[(T_i^{n+1})^4 - T_\infty^4\right] + U_\infty LWC_\infty \beta Cp_w T_c - \dot{m}_{evap} Cp_w T_c.$$

An explicit time marching scheme can be used to solve equations (24) and (25) for all icing regions, where the previous time step n solution is used to evaluate the next time step ($n+1$). By using eigenvalues (22), the time step can be written as,

$$\Delta t = \sigma \frac{\Omega}{\Lambda}, \text{where } \Lambda = \frac{h_f \tau}{\mu_w}.$$

(26)

For a given time span Δt, the volume of ice accretion can be expressed as,

$$V_{ice} = \int_0^{\Delta t} \int_S \frac{\dot{m}_{ice}}{\rho_{ice}} dSdt.$$

(27)

For a single surface $dS(t)$ of area $A_{surface}$, the ice thickness (h_{ice}) can be given as,

$$h_{ice} = \frac{\dot{m}_{ice} \Delta t}{\rho_{ice} A_{surface}}.$$

(28)

The calculated ice thickness and the surface normal vector are then linearly interpolated to adjacent node points, and the newly formed surface is generated by the interpolated node values. The ice thickness determined this way was added to each successive time step to find the total thickness of ice accretion. Finally, the new node points were used for re-meshing and grid movement.

3. Methodology for sensitivity analysis

Global sensitivity analysis (GSA) is an important approach to quantify the significance of all input parameters with respect to model output [49, 50]. There is a wide range of global sensitivity analysis approaches available for different kinds of problems [51, 52]. In general, all the proposed GSA approaches can be categorized into the analysis of variance (ANOVA), decomposition of the response variance [49], and the derivative-based method. The ANOVA method decomposes the variance of the output as a sum of the contributions of each input parameter. Sobol's sensitivity indices (SSIs) are used to quantify the fractional contribution of each input parameter [49]. On the other hand, the derivative-based method focuses on the total influence of the parameters. However, the high computational cost of the method limits its practical application to computationally intensive analyses [53]. Further, because of

16

their low computational costs, sampling-based or surrogate-based (metamodel) GSA approaches can be used for engineering studies. The sampling-based approaches [54] can significantly improve the performance of the GSA approach by using a low discrepancy sequence (e.g., the Sobol sequence).

In the surrogate-based approach, a metamodel is constructed to evaluate the sensitivity indices using quasi-Monte Carlo or Sobol's methods. Metamodels such as Kriging [55], Gaussian process [56], or the radial basis function (RBF) [57] can be utilized to construct the model. In addition, to reduce the computation cost of GSA, the polynomial chaos expansion method [38] is often used to construct the surrogate model. The sensitivity indices of a metamodel can be evaluated using an analytical method based on the orthogonal polynomial interpolation surrogate model. However, such models are not suitable for high dimensional and highly non-linear problems.

In the present study, in order to overcome these problems, the RBF and Sobol's methods were used to construct the metamodel and evaluate the sensitivity indices, respectively.

3.1. Sampling based on low discrepancy Sobol sequence

A sensitivity analysis generally involves the design of sampling points, the construction of metamodels, and the evaluation of sensitivity indices. Sampling, which is a process of exploring the design space, plays a significant role in the distribution of design points in the given space. The sample size also plays a vital role in the construction of models. Hence, the selection of a sampling strategy becomes an important step in the sensitivity analysis.

There are several sampling methods, including the pseudo-random, stratified, Latin hypercube sampling (LHS), Hammersley, and Sobol sequence [58]. In the present study, the Sobol sequence was used mainly for its low discrepancy sampling capability. The Sobol sequence belongs to the quasi-random sampling method category. Figure 4 shows three sampled parameters plotted against each other in pairs using a Sobol sequence for variables x_1, x_2, and x_3. A sampling method based on a Sobol sequence can evenly distribute the design points in each domain. Its discrepancy in the exploration of multidimensional parameter space is known to be lower than other sampling techniques [58]. Moreover, sampling methods

17

based on a Sobol sequence can converge to the true mean faster than other methods. In the present investigation, the sampling points were generated with five variables (parameters) using a Sobol sequence.
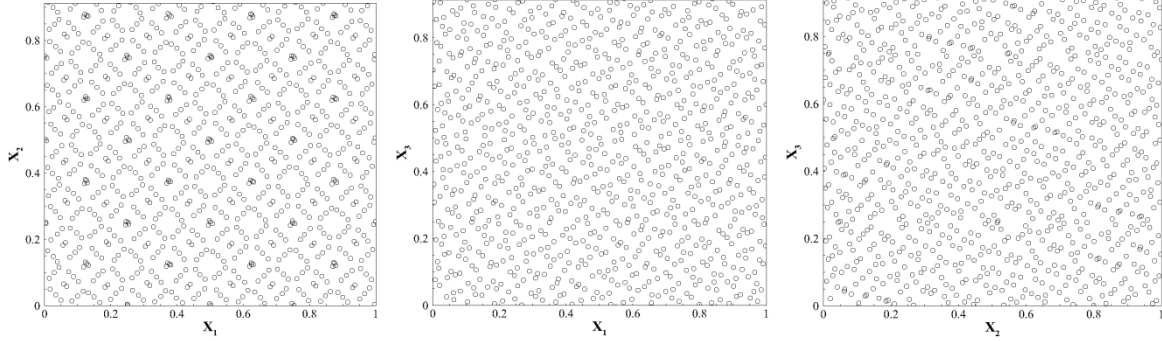

Fig. 4. Three sampled parameters plotted against each other in pairs using Sobol' sequence. Left to right: x_1 vs x_2, x_1 vs x_3, and x_2 vs x_3.

3.2 Metamodeling using RBF

Metamodeling is the process of approximating a system from a limited number of selected samples generated by the system. The RBF method was initially developed to fit the irregular topographic contours of geographical data [59]. It produced excellent fits to arbitrary contours of both deterministic and stochastic response functions. The RBF can be expressed as,

$$Y = F(\boldsymbol{x}) = \sum_{n=1}^{N} w_n \boldsymbol{\varphi}\left(\|\boldsymbol{x} - \boldsymbol{x_n}\|\right) \tag{29}$$

where $\boldsymbol{\varphi}$, $\boldsymbol{x}$, and $\boldsymbol{x}_n$ represent the vector of the basis function, design variables, and the vector of design variables at the nth sampling point, respectively. w_n and $\|\boldsymbol{x} - \boldsymbol{x_n}\|$ are the unknown coefficient of the nth basis function and the Euclidean norm, respectively. The approximate function Y is calculated at n-dimensional sample point $\boldsymbol{x}_n$ selected by Sobol sequence in the design domain. The coefficient w can be determined as follows,

$$w = A^{-1}\boldsymbol{F} \tag{30}$$

where

$$w = \begin{bmatrix} w_1 \\ w_2 \\ \vdots \\ w_N \end{bmatrix}, \quad A = \begin{bmatrix} \varphi_{11} & \varphi_{12} & \cdots & \varphi_{1,N} \\ \varphi_{21} & \varphi_{22} & \cdots & \varphi_{2N} \\ \vdots & \vdots & \ddots & \vdots \\ \varphi_{N1} & \varphi_{N2} & \cdots & \varphi_{NN} \end{bmatrix}, \quad F = \begin{bmatrix} f_1 \\ f_2 \\ \vdots \\ f_N \end{bmatrix}. \tag{31}$$

3.3 Sobol's sensitivity indices (SSIs)

A global sensitivity analysis can be performed on the basis of Sobol's decomposition of the computational model F, which can be written as,

$$F(\boldsymbol{x}) = F_0 + \sum_{N=1}^{n} F_N(\boldsymbol{x}_N) + \sum_{1 \leq N < M \leq n} F_{NM}(\boldsymbol{x}_N, \boldsymbol{x}_M) + \cdots + F_{12\ldots n}(\boldsymbol{x}). \tag{32}$$

Here F_0 is a constant, F_N is a function of x_N, and F_{NM} is a function of x_N and x_M. If the following orthogonality condition is enforced,

$$\int_0^1 F_{N_1 N_2 \ldots N_s}(\boldsymbol{x}_{N_1}, \boldsymbol{x}_{N_2}, \ldots, \boldsymbol{x}_{N_s}) d\boldsymbol{x}_k = 0, \quad \text{for } k = N_1, N_2, \ldots, N_s, \tag{33}$$

and, when the terms in the decomposition are constructed as follows,

$$\begin{aligned} F_0 &= \int F(\boldsymbol{x}) d\boldsymbol{x}, \\ F_N(\boldsymbol{x}_N) &= \int F(\boldsymbol{x}) \prod_{K \neq N} d\boldsymbol{x}_K - F_0, \\ F_{NM}(\boldsymbol{x}_N, \boldsymbol{x}_M) &= \int F(\boldsymbol{x}) \prod_{K \neq M, N} d\boldsymbol{x}_K - F_0 - F_N(\boldsymbol{x}_N) - F_M(\boldsymbol{x}_M). \end{aligned} \tag{34}$$

the decomposition (32) is called the ANOVA. Now the variance (D) of $F(\boldsymbol{x})$ can be written as,

$$D = \int F(\boldsymbol{x})^2 d\boldsymbol{x} - F_0^2. \tag{35}$$

Due to the orthogonality property of the decomposition, squaring both sides of equation (32) and integration yield the following relation,

$$D = \sum_{i=1}^{k} D_i + \sum_{i < j} D_{ij} + \ldots + D_{1,2,\ldots,k}. \tag{36}$$

In this expression, the partial variance corresponding to the subset of parameters, $D_{i_1 \ldots i_s}$, which is defined

as $\int F_{i_1 \ldots i_2}^2(x_{i_1}, \ldots, x_{i_s}) dx_{i_1}, \ldots, x_{i_s}$, is the variance of $F_{i_1 \ldots i_s}(x_{i_1}, \ldots, x_{i_s})$.

The SSIs for the corresponding subset of parameters can be defined as,

$$S_{i_1 \ldots i_s} = \frac{D_{i_1 \ldots i_s}}{D}. \tag{37}$$

The first-order contribution (main effect) of any variable x_i can then be calculated as,

$$S_i = \frac{D_i}{D}. \tag{38}$$

Moreover, the second-order contribution (interaction effect) can be expressed as,

$$S_{ij} = \frac{D_{ij}}{D}. \tag{39}$$

Finally, the total sensitivity indices can be given as,

$$S_{Ti} = S_i + \underset{i \neq j}{S_{ij}} + \cdots + S_{1 \ldots i \ldots s}. \tag{40}$$

The first-order sensitivity indices measure the fractional contribution of a single parameter to the output variance, while the second-order sensitivity indices measure the parameter interactions to the output variance. The total sensitivity indices are the sum of first-order, second-order, and higher-order effects. Sensitivity indices with a higher value indicate the higher influence of the parameters in the model.

4. Results and discussions: Effects of critical physical and modeling parameters on ice accretion and aerodynamic performance degradation

4.1 Verification and validation of computational models

To verify the computational models, three different meshes were used. From Fig. 5 of the pressure coefficient distributions, it can be observed that mesh-2 is very close to the asymptotic regime, justifying the use of mesh-2 for subsequent calculations. The maximum Y+ value corresponding to mesh-2 was set to 1.0.
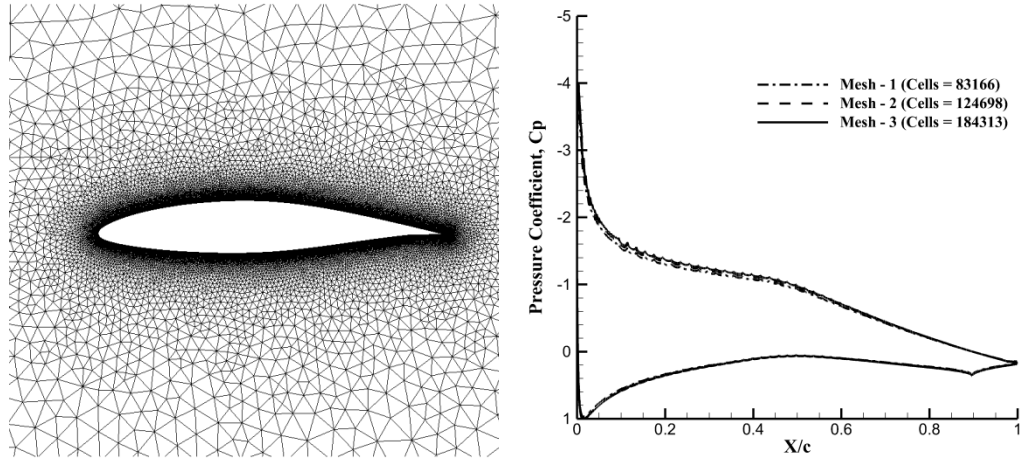
Fig. 5. Grid distribution (left) and pressure coefficient (right) around the NACA65$_2$-415 airfoil at $\alpha = 8^o$, $M = 0.23$, Re = 4.9 million.

To validate the air flow solver, the computed pressure coefficients over a NACA65$_2$-415 airfoil were compared with the experimental data, as shown in Fig. 6 (left). The experiment was conducted for a 0.9144 m chord airfoil model from NASA [11]. The test was conducted at a Mach number of 0.23, an angle of attack of 8^0, and Reynolds number of 5.2 million. The convective heat transfer coefficients were compared with the LEWICE results over a NACA0012 airfoil at Mach number of 0.32, an angle of attack of 4^0, and temperature 262.04 K, as shown in Fig. 6 (right).

To validate the droplet solver, the distributions of the computed collection efficiencies of droplets were compared with the experimental data from NASA for an LWC of 1.0 g/m^3 and MVD of 21 µm, as shown in Fig. 7. Finally, the ice accretion shapes on NACA0012 for rime ice, glaze ice, and glaze horn ice cases were validated against the experiment data [4] for icing conditions summarized in Table 1, as shown in Fig. 8 (a), (b), and (c), respectively. Overall, the computed results were found to be in qualitative agreement with the experimental data.
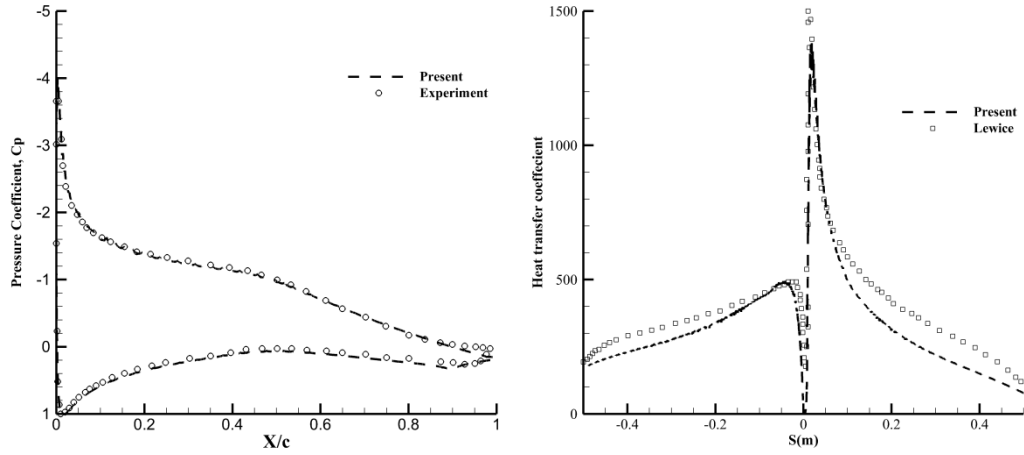
Fig. 6. Pressure coefficient (left) over the NACA65$_2$-415 airfoil at α = 8°, M = 0.23, Re = 4.9 million and the convective heat transfer coefficient (right) over a NACA0012 airfoil at α = 4°, M = 0.32, T = 262.04 K.

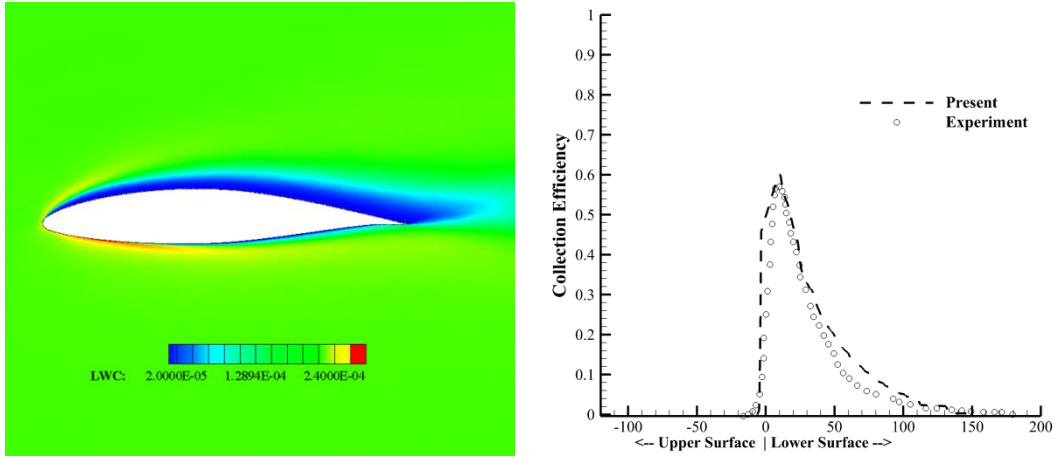**Fig. 7.** LWC contour (left) and collection efficiency (right) around the NACA65$_2$-415 airfoil at α = 8°, M = 0.23, LWC = 1.0 g/m^3, MVD = 21 μm.

Table 1 Meteorological and flight conditions for validation of ice accretion on NACA0012 airfoil.

Parameter	Rime ice	Glaze ice (Case 1)	Glaze ice (Case 2)
V_∞ , m/s	102.8	102.8	102.8
T_∞ , K	250.3	262.04	263.71
α , deg	4	4	4
LWC, g/m^3	0.55	0.55	0.55
MVD, μm	20	20	20
Time, s	420	420	420
Chord, m	0.5334	0.9144	0.5334
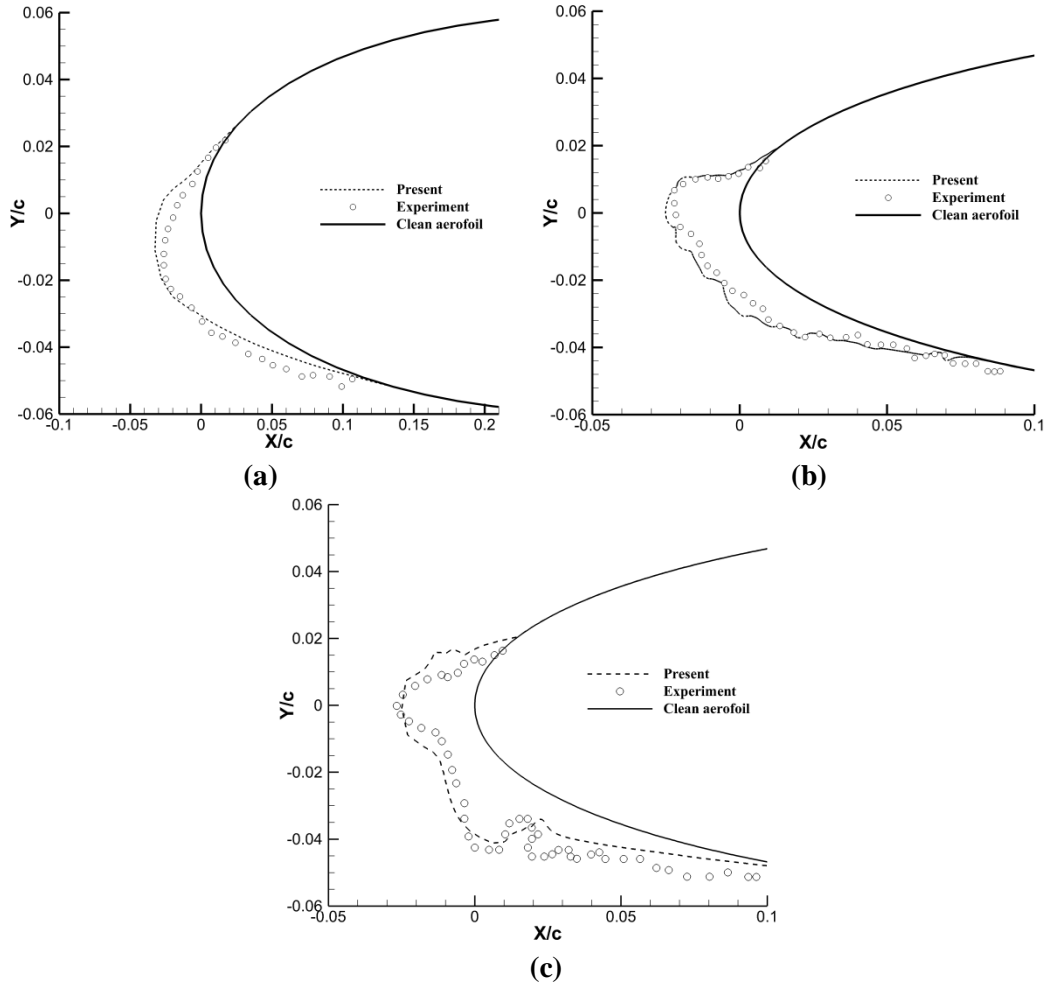
Fig. 8. Comparison of ice accretion results with NASA IRT experimental data on an NACA0012 airfoil at the meteorological and flight conditions shown in Table 1: (a) rime ice, (b) glaze ice (case 1), and (c) glaze ice (case 2).

4.2 Effects of critical physical and modeling parameters on ice accretion

4.2.1 Surface roughness

Shear stress and heat flux over the airfoil surface can change abruptly with varying surface roughness. In particular, the heat transfer coefficient is actively involved in the convective and evaporative cooling, so that the direct impact of surface roughness can be easily observed in ice accretion shapes, as demonstrated in Fig. 9. Increasing surface roughness enhances the surface heat flux, resulting in an increase in ice accretion potential.
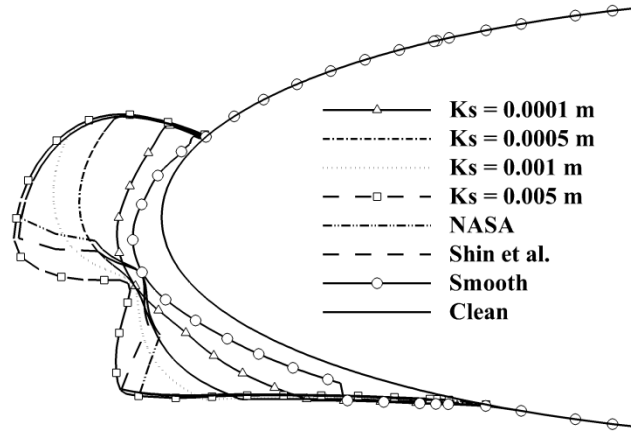
Fig. 9. Ice shape for various roughness (*Ks*) at α = 4°, M = 0.316, T = 262.4K, LWC = 1.0 g/m³, MVD = 20 μm, exposure time = 231 Sec, and chord = 0.5334 m.

Figure 9 shows horn ice formation at the leading edge with increasing surface roughness. This is the main reason why the accelerated ice accumulation is observed after an aircraft surface forms initial roughness. The upper limit of the roughness range in this study was chosen based on the surface roughness model calculated by Ruff *et al*. [29] and Shin *et al.* [30].

4.2.2 Ice density

In icing wind tunnel and natural flight tests, the measured ice density may not be equal to 917 kg/m³. In fact, the density of ice accreted on an aircraft surface is known to widely vary and be as low as 400 kg/m³. As illustrated in Fig. 10, the ice thickness and shape are strongly influenced by ice density, which is inversely proportional to volume at constant mass.
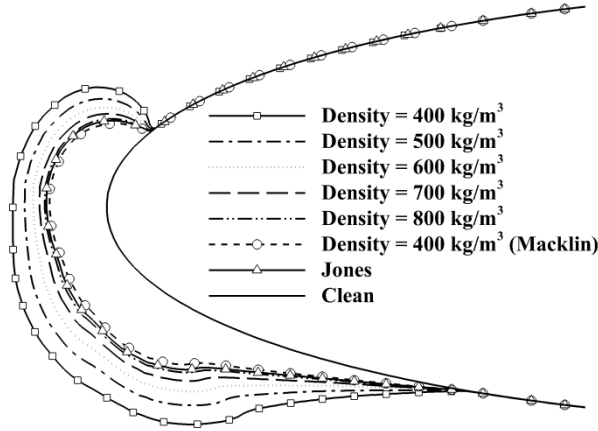
Fig. 10. Ice shape with various ice density at α = 4°, M = 0.316, T = 262.04K, LWC = 0.55 g/m³, MVD = 20 μm, exposure time = 420 Sec, and chord = 0.9144 m.

In computational simulations of ice accretion, empirical formulas are often introduced to address ice density; for example, models by Macklin [31] and Jones [32]. In these empirical formulations, the ice density is determined in terms of droplet impact velocity, MVD, and surface temperature. In computational simulations, the density is derived from the computed surface temperature, since the droplet properties are assumed to be constant under the quasi-unsteady assumption. For instance, the formulas by Macklin and Jones yield ice densities of 900 kg/m³ and 800 kg/m³, respectively.

4.2.3 Single shot and multi-shot

In the single-shot method, the ice shape is computed solely on the initial (one-time) air flow field and droplet solution, which is applied for the entire exposure time, without any mesh deformation to take ice growth into account. On the other hand, in the multi-shot method, the air flow field and droplet solution are updated after a certain number of ice accretion time steps and automatic grid regenerations. A full unsteady time-accurate method is also possible in principle, but has yet to be developed, since it requires overcoming the need for an enormous amount of computing power. The multi-shot method under the quasi-steady assumption is more accurate than the single-shot method, but there is no thumb rule to select the number of shots for best predictions.
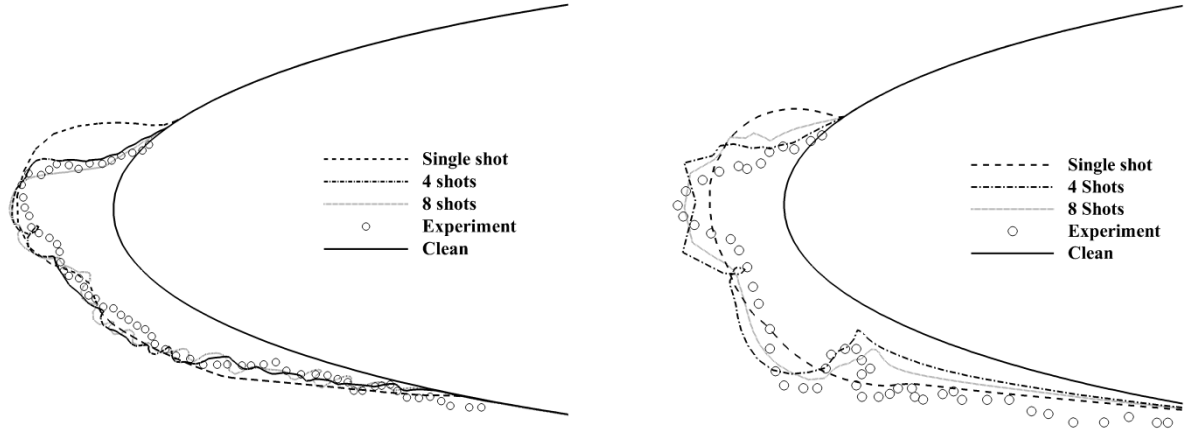
Fig. 11. Ice shape predicted by multi-shot approach: case 1 (left) and case 2 (right) of glaze ice summarized in Table 1.

Figure 11 highlights the differences in ice shape produced by the single and multi-shot methods. Because it updates the air and droplet solutions after certain ice accretion time steps during the simulation, the multi-shot method more accurately predicts the shapes (non-smooth and horn) of the ice than the single shot method. Generally, for *n* number of shots, the computational cost is *n* times higher than a single shot calculation. This hinders the wide application of the multi-shot method for real world problems.

4.2.4 Droplet distribution

Figure 12 highlights the differences in ice shape produced by the mono-disperse and poly-disperse Langmuir-D droplet distributions. The droplet equations were first solved for each bin of droplets corresponding to a specific droplet diameter. The collection efficiency of each bin of droplets (βi) was then combined into a single distribution to determine the total collection efficiency via the sum of multiplication of the fraction of the LWC, and the collection efficiency of each bin of droplets.
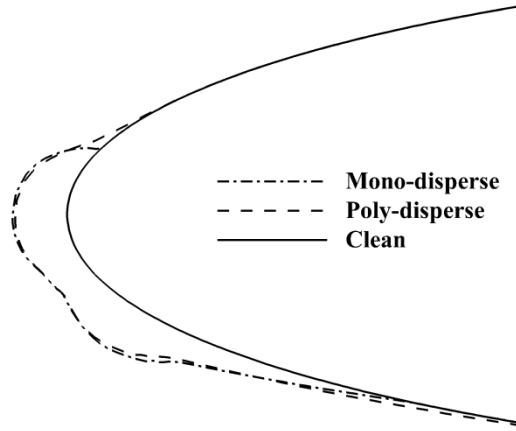
Fig. 12. Ice shape with and without droplet distribution at α = 4°, M = 0.316, T = 262.04K, LWC = 0.55 g/m³, MVD = 20 μm, exposure time = 420 Sec, and chord = 0.9144 m.

In general, the poly-dispersed droplet distribution broadens the impingement limits, since droplets in the low and high end of the droplet distribution tend to bring more diverse impingement patterns. In rime ice conditions, the ice accretion limit is determined directly by the impingement limit. In contrast, under glaze ice conditions, the ice accretion limit is determined by the runback of water film beyond the impingement limit. This fact can be confirmed from Fig. 12, which shows the poly-dispersed droplet distribution broadens the ice accretion limit; in particular, at the upper surface of the airfoil.

4.2.5 Evaporation

Evaporative heat transfer is one of the major cooling parameters affecting the ice accretion mass and shape, next to well-known convective cooling. Using the Chilton and Colburn analogy [60], the evaporative mass loss can be determined as a function of the mass transfer coefficient by diffusion. Only a small fraction of liquid water covering the surface evaporates in the air. The mass loss by evaporation can be expressed as,

$$\dot{m}_{evap} = h_{dif}\left(\rho_{vs} - \rho_{ve}\right)A, \quad h_{dif} = \frac{h_c}{\rho_a C_{p,a} Le^{2/3}}, \quad Le = \frac{k_a}{\rho_a C_{p,a} D_{va}}. \tag{41}$$

Here, h_{dif} is the mass transfer coefficient, ρ_{vs} is the saturated water vapor density at the surface temperature, ρ_{ve} is the water vapor density at the temperature at the edge of the boundary layer, A is the

area of the surface, *Le* is the Lewis number, K_a is the thermal conductivity air, and D_{va} is the water vapor diffusion coefficient in the air.
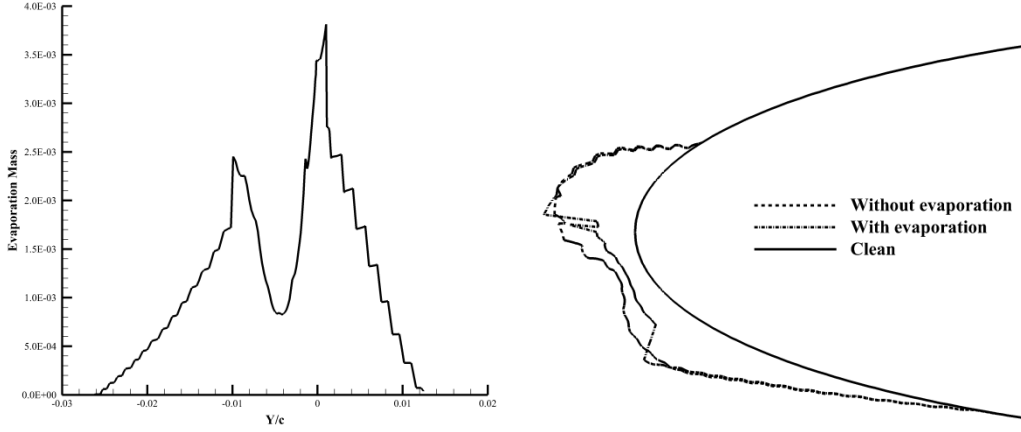

Fig. 13. Evaporation mass (left) and ice shape with and without evaporation (right) at $\alpha = 4^{\circ}$, M = 0.316, T = 262.4K, LWC = 1 g/m^3, MVD = 20 μm, exposure time = 231 Sec, and chord = 0.5334 m.

In Fig. 13, the instant evaporation mass (left) is shown, along with the ice shape (right) with and without evaporation mass loss. The results show that the evaporation mass locally and substantially changes on the surface of the airfoil for a given icing condition. The evaporation mass is high at the leading edge and reduced to zero in the aft positions. These changes in evaporation mass may be due to the variation in heat transfer coefficients and the different levels of available liquid film. The effect of varying evaporation mass can be observed; for example, the ice thickness near the stagnation point of the leading edge was significantly reduced.

4.3 Sensitivity analysis on the critical physical and modeling parameters based on Sobol's method

In the previous section, the effects of each critical physical and modeling parameters were discussed, which naturally leads to a question about the sensitivity of the ice shape on each parameter. However, in order to obtain deep insight into the most influential (or insignificant) parameters, the interaction effects of the parameters also need to be addressed.

Table 2 Range of physical and modeling parameters.

Parameter	Minimum	Maximum
Roughness, m	0.0001	0.005
Ice density, Kg/m^3	400	917
Number of shots	1	12

For this purpose, a sensitivity analysis was conducted on the critical physical and modeling parameters. The range of critical parameters considered in the current investigation is summarized in Table 2. The sampling points were generated using a Sobol sequence, and the RBF metamodeling technique was used to generate the model of the system. The accuracy of the metamodeling should be verified before determining sensitivity indices. To measure the metamodel accuracy, R square was used, which can be expressed as,

$$R^2 = 1 - \frac{\sum_{i=1}^{n}(y_i - \hat{y}_i)^2}{\sum_{i=1}^{n}(y_i - \bar{y}_i)^2} = 1 - \frac{\text{Mean Square Error}}{\text{Variance}}, \tag{42}$$

where $\hat{y}_i$ is the predicted value for the observed value y_i, $\bar{y}_i$ is the mean variance of the observed values. A larger R square value indicates a more accurate (overall) metamodel. The current RBF metamodeling yielded a metamodel with an R square value of 0.9463, which is suitable for calculating the sensitivity indices.

4.3.1 First-order and total sensitivity indices of critical physical and modeling parameters

The first-order and total effect of parameters were evaluated using equations (38) and (40). The first-order and total contributions of roughness on ice attributes are illustrated in Fig. 14 (left). The ice horn position (P_{upper}) and ice horn angle (θ_{upper}) are significantly affected by roughness. The roughness contributes to the total effect, accounting for more than 65% in the determination of ice horn position, and approximately 60% in the determination of ice horn angle. On the other hand, the contribution of roughness to the ice accretion limit (S_{upper} and S_{lower}) and mass was negligible in the first-order effect.

However, in terms of total sensitivity indices, the contribution of the roughness increased for all ice attributes, including ice mass.

Figure 14 (right) shows that ice mass and ice height (H_{upper} and H_{lower}) are critically affected by ice density, while the other attributes are negligible. The total sensitivity indices illustrate that the ice density contributes approximately 60% in determining the ice mass and ice horn height on the upper surface (H_{upper}). This implies that the mass of ice changes substantially together with the ice horn height, if the ice density varies with given icing conditions. This feature should be considered when modeling ice accretion and in the accurate measurement of ice mass in the certification process.
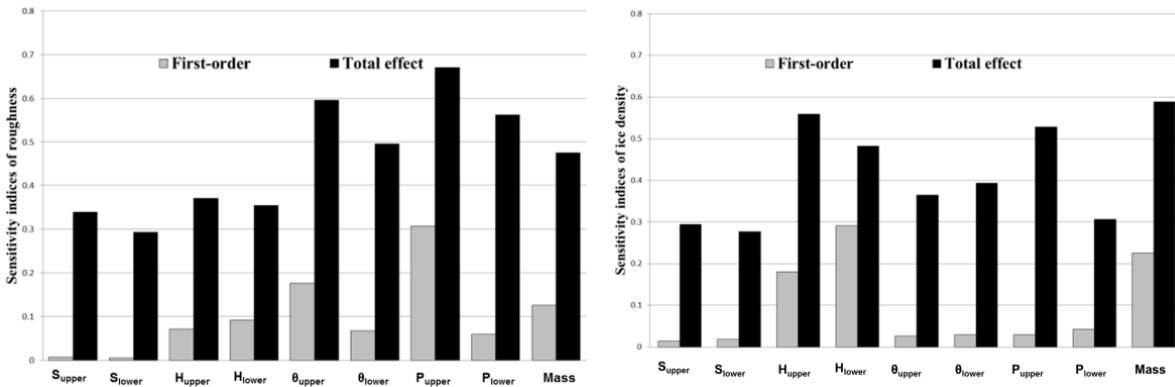

Fig. 14. Sensitivity indices of roughness (left) and ice density (right) on eight ice geometry attributes and mass.
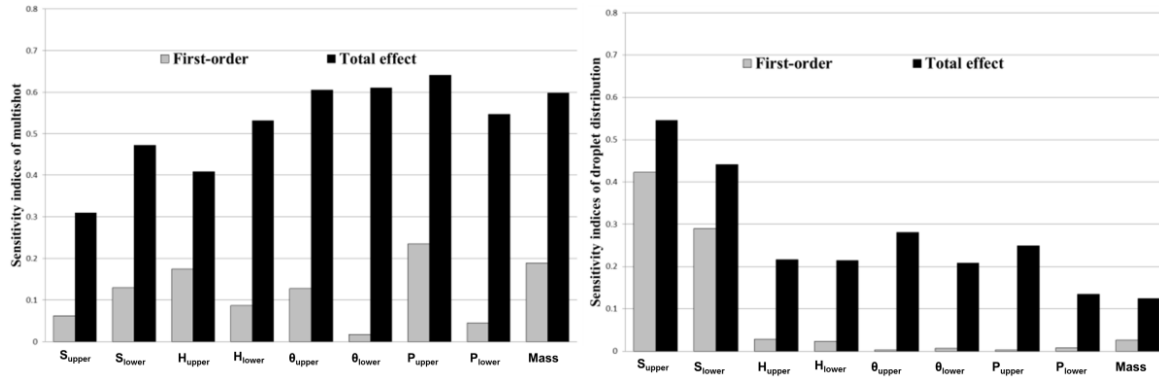

Fig. 15. Sensitivity indices of number of shots (left) and droplet distribution (right) on eight ice geometry attributes and mass.
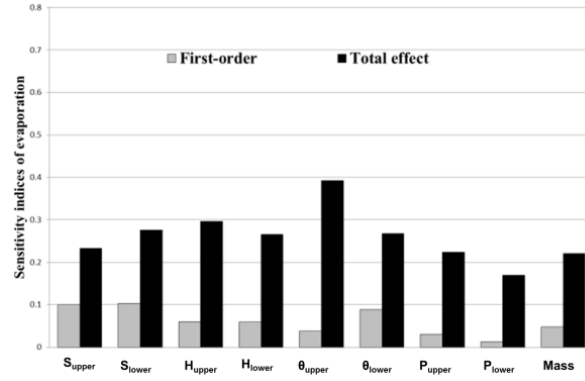
Fig. 16. Sensitivity indices of evaporation model on eight ice geometry attributes and mass.

The first-order and total contribution of the number of shots on ice attributes is illustrated in Fig. 15 (left). In the first-order effect, the number of shots contributes more to the upper horn position (P_{upper}), the upper horn height (H_{upper}), and ice mass. In case of total effect, the number of shots contributes significantly to most of the ice attributes, including ice horn position and angle (60%). It is also notable that the total sensitivity indices of ice mass increase significantly. All these results indicate the extreme importance of the number of shots in the ice accretion simulation.

Figure 15 (right) shows that the main contribution of droplet distribution is to the ice accretion limit (S_{upper} and S_{lower}). However, the total sensitivity indices show that other ice attributes are also affected by droplet distribution to some degree, because of interactions.

The first-order and total contribution of the evaporation model to ice attributes is illustrated in Fig. 16. The first-order effect of the evaporation model is distributed evenly among the icing attributes. Note that the ice accretion limit (S_{upper} and S_{lower}) is affected by the evaporation model. The total sensitivity indices show that the evaporation model affects the ice horn angle (θ_{upper}) most.

It will also be instructive to compare the sum of the first-order and total effects for five critical physical and modeling parameters. According to the sensitivity indices shown in Figs. 14-16, the sum of the first-order and total effects, respectively, were found to be in the following order: number of shots (0.9642, 4.721), surface roughness (0.9108, 4.156), ice density (0.857, 3.794), droplet distribution (0.8116, 2.417), and evaporation (0.5385, 2.344). It should be mentioned that, because of the interactions, the sum

of the first-order effects in the case of a nonlinear model is not necessarily equal to 1.0. These results indicate that the number of shots and surface roughness are the most critical physical and modeling parameters in nonlinear ice accretion, followed by ice density and poly-disperse droplet distribution, and lastly by evaporation model.

4.3.2 Influence of critical physical and modeling parameters on ice shape attributes

It was well known that ice accretion on the lower surface of an airfoil has a minimal effect on airfoil performance degradation [61]. In this study, the contribution of critical parameters was further investigated with a focus on ice attributes on the upper surface of an airfoil. The so-called *normal probability plot of the effects* (or *plot of the effects*, in short) can be used to determine the influence (level and direction) of the critical parameters on ice attributes.

The normal probability plots of the effects are presented in relation to the standardized effects in Figs. 17-21. Parameters (or factors) that do not significantly influence the responses lie close to the distribution fit line, originating at (0, 50) in the plots. Parameters that influence the responses positively are located on the right of the distribution fit line, while ones that influence the responses negatively are located on the left of the distribution fit line. The further from the distribution fit line on the *x*-axis, the greater is the effect on the responses (and then the corresponding parameters are judged statistically significant). The interactions of different parameters were also investigated to better understand the interaction effects.

Figure 17 shows the parameters and their interactions (like ABC) that influence the ice accretion limit on the upper surface of an airfoil (S_{upper}). The significance of those parameters was found to be in the following order: the droplet distribution (D), the interaction of droplet distribution with evaporation (DE), the evaporation model (E), and the interaction of roughness, number of shots, and droplet distribution (ACD). Other parameters showed insignificant effects on S_{upper}. Note that ice density (B) does not appear in the plot, indicating the diminishing role of ice density in this case.
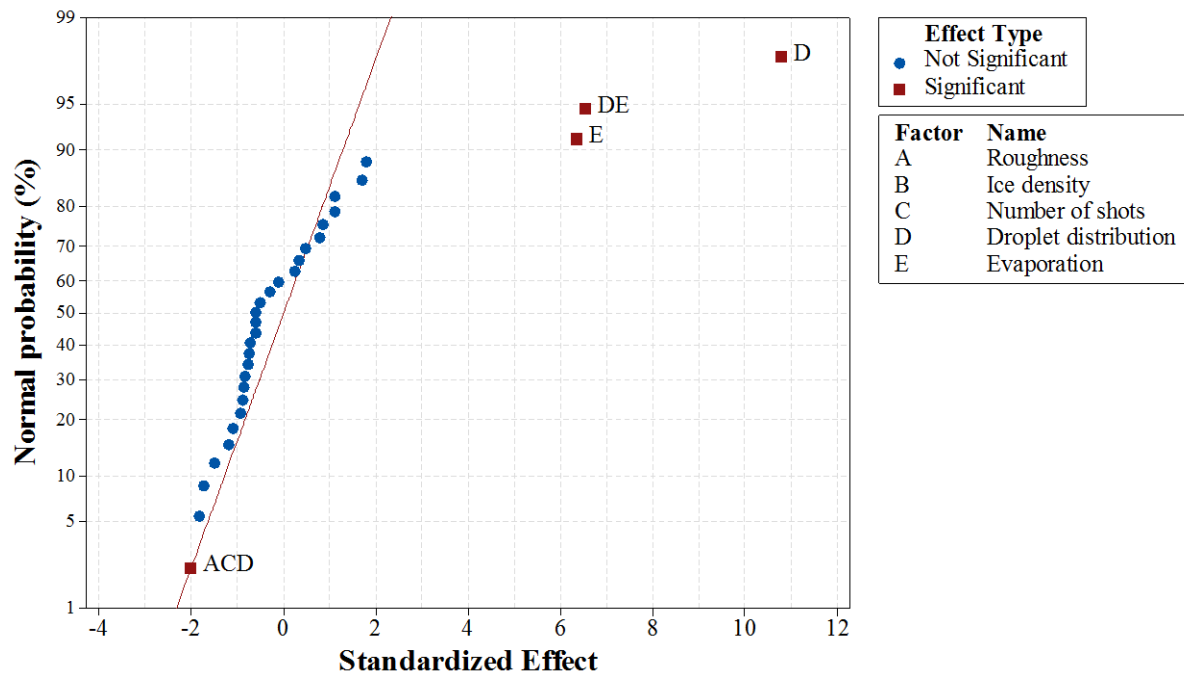
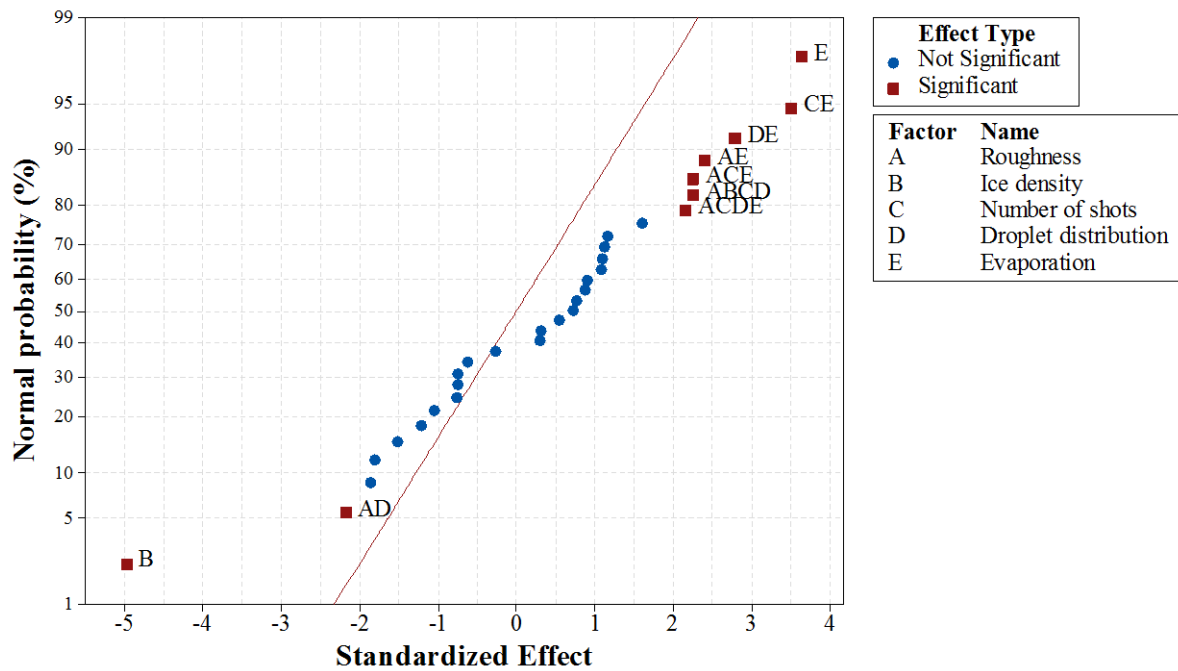**Fig. 17.** Significance of parameters on the upper surface icing limit (S_{upper}).

Fig. 18. Significance of parameters on the upper surface ice height (H_{upper}).

Figure 18 shows the parameters and their interactions that influence the ice horn height on the upper surface of an airfoil (H_{upper}). Ice density (B) was found to be the dominant factor in determining the ice

horn height, with the highest negative influence (furthest to the distribution fit line), meaning that an increase in ice density will decrease the ice horn height significantly. The interaction in the number of shots and evaporation (CE) had the second largest influence on ice horn height. The combined effect of continuous updates of air and droplet flows in the multi-shot method, and the removal of some mass of water film from the stagnation region by activation of evaporation may lead to an increase of ice horn height. The activation of evaporation (E) also has a strong positive influence on the ice height, since it generally removes some mass of water film from the ice accretion region. It thus substantially affects the thickness of ice accretion and the ice horn height.
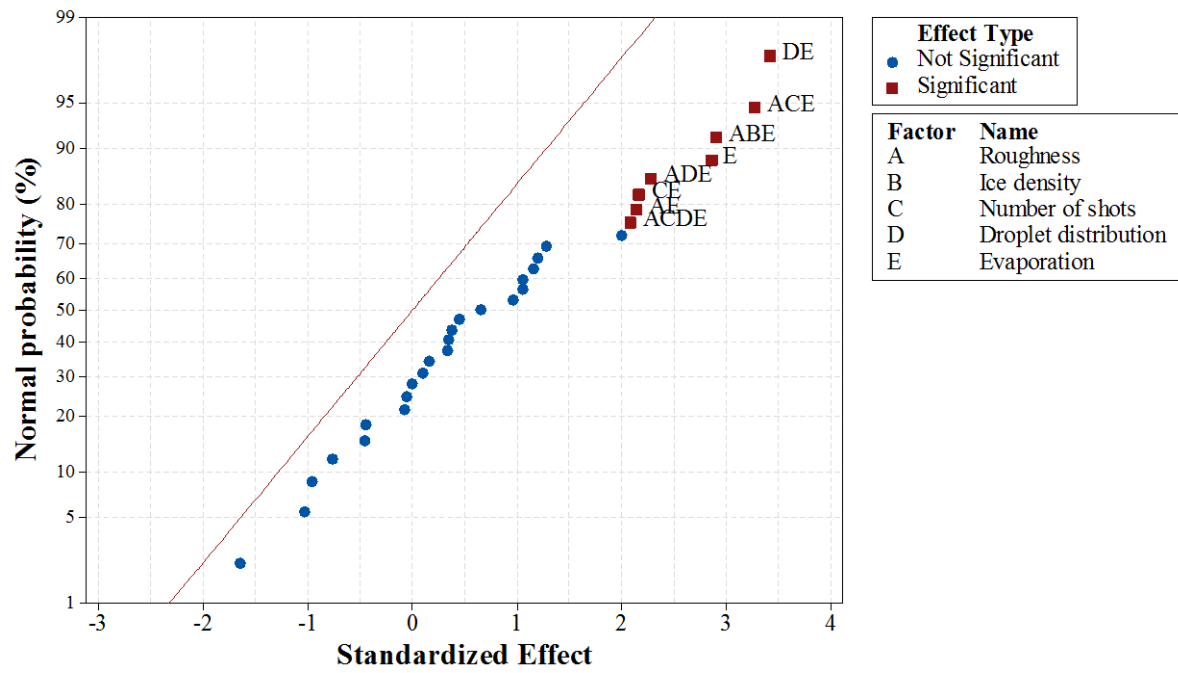
Fig. 19. Significance of parameters on the upper surface ice horn angle (θ_{upper}).
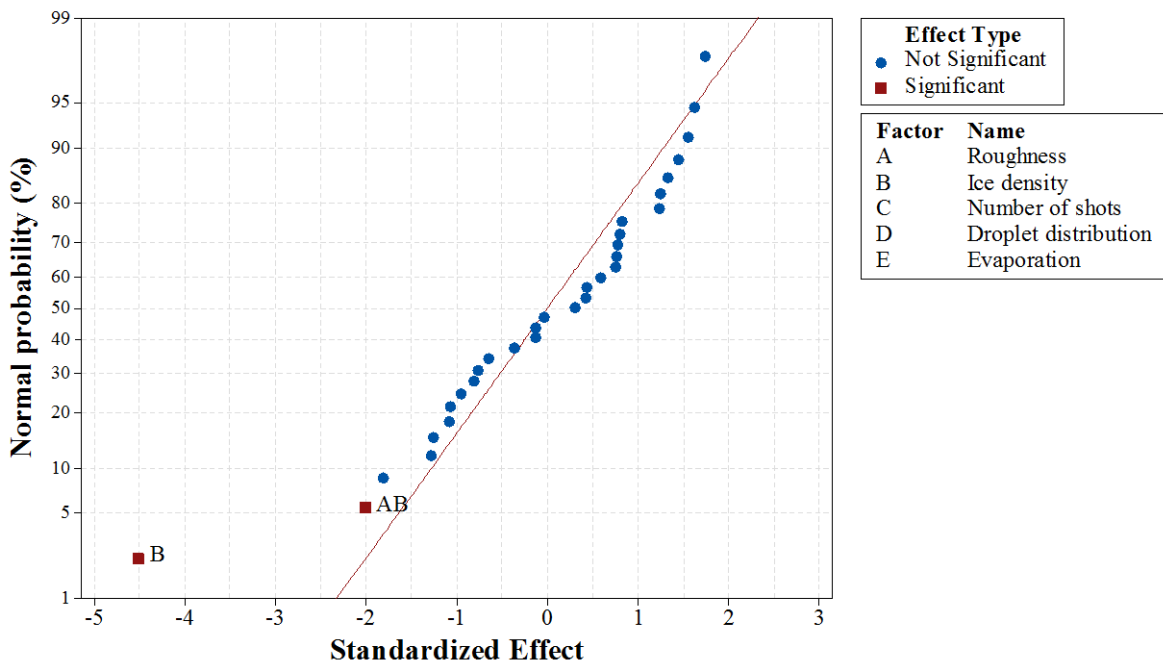

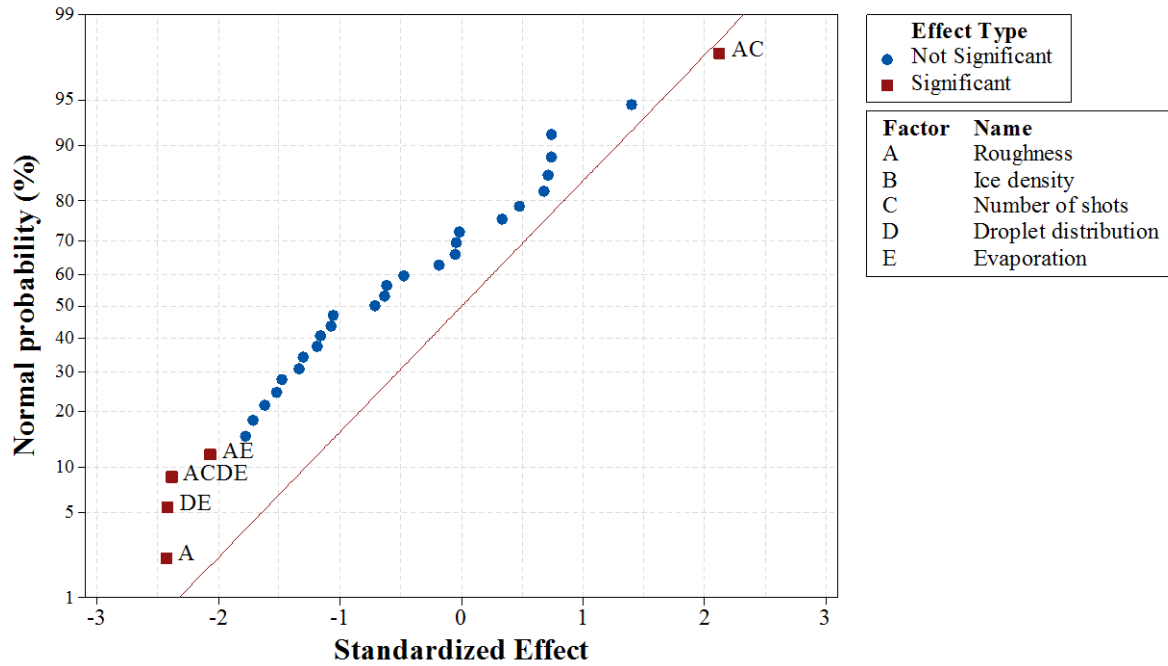**Fig. 20.** Significance of parameters on ice accumulation mass.

Fig. 21. Significance of parameters on the upper surface ice horn position (P_{upper}).

Figure 19 shows the significance of parameters on the ice horn angle on the upper surface of an airfoil (θ_{upper}). The plot of the effects illustrates that, as expected from the sensitivity index of evaporation on the total effect of θ_{upper} in Fig. 16, the activation of evaporation (E) has a strong positive influence on the ice horn angle. Interestingly, its influence is exerted by various forms of multiple interactions like AE, CE, DE, ABE, ACE, ADE, and ACDE, but not by itself.

Figure 20 shows the significance of parameters on the ice mass. As expected, the ice density (B) has the strongest negative influence on ice mass. The mutual interaction of surface roughness and ice density (AB) was also found to contribute significantly to ice mass. A possible explanation for this result may be that the surface roughness affects the heat flux and convective cooling, resulting in a change in ice accretion and a negative influence on ice mass when combined with the ice density effect.

Finally, the significance of parameters on the ice horn position on the upper surface of an airfoil (P_{upper}) is shown in Fig. 21. Surface roughness (A) was the main factor which affects the ice horn position, and the interaction of other parameters (AC, AE, DE, and ACDE) also had a significant influence on the ice horn position. The influence of roughness on the ice horn position was negative, meaning that the increase

36

in roughness moves the ice horn position towards the leading edge of the airfoil. Further, the interaction of roughness and the number of shots (AC) had a significant influence on the ice horn position. An increase in roughness and the number of shots can move the ice horn position from the leading edge towards the aft location of the airfoil. However, ice density (B) does not appear in the plot, indicating the insignificance of ice density in this case.

Overall, the number of shots and roughness turned out to be the most critical physical and modeling parameters in the nonlinear ice accretion process, as characterized by ice horn height, ice horn angle, and ice horn position. In a multi-shot ice accretion simulation, the air flow field and droplet solutions are updated after a certain number of ice accretion time steps. After the grid automatically regenerates to reflect the change in ice shape, the shear stress, heat flux, and pressure on the surface are recalculated on new grids. The collection efficiency and impact velocity of droplets are then updated by droplet solver. This multi-shot simulation will produce more realistic ice shapes than a single shot simulation.

Interestingly, the number of shots was found to have higher interaction effects than the main effects, as confirmed by its appearance in multiple interactions, like AC, AD, AE, ABE, ACE, ADE, ABCE, and ACDE, far more than as a single entity A. This feature can be supported by the highest value in interaction effects (3.757) in Fig. 15 (left), which represents the deviation between the total effects (4.721) and the first-order effect (0.9642). A possible explanation for this property may be that the number of shots affects all ice accretion processes through the multiple updates of the air flow field, droplet solution, and ice shape.

Surface roughness affects the ice horn height and ice horn position through the strong connection between roughness and heat flux. The increase in roughness increases the heat transfer coefficient significantly, which in turn increases the convective cooling and accretion of ice. Accurate calculation of heat flux is thus essential to accurately predict ice shapes. Ice density and droplet distribution also affect ice mass and the ice accretion limit. Droplet distribution affects the droplet impingement limit, which can

directly affect the ice accretion limit. Hence, proper ice density and droplet distribution models are recommended to accurately model ice accretion and ice protection systems.

4.4. Effects of roughness, ice density, and multi-shot on aerodynamic performance degradation

Understanding the effects of ice accretion on aerodynamic performance is critical when operating aircraft in icing conditions and designing ice protection systems. For example, initial in-flight ice may be present on all unprotected and protected surfaces during the activation time of ice protection systems. In addition, large in-flight ice may be present on all surfaces in the event of a system failure. In the latter case, the most critical factor to be considered is the ice shape that has accumulated during the time needed to exit icing conditions (usually about 22.5 minutes) within the icing envelope, which results in the largest adverse effects on aerodynamic performance over the applicable phases of flight of the aircraft.

In this context, the effects of critical physical and modeling parameters on the aerodynamic performance degradation of airfoils were investigated by unified computational solvers for air, droplet impingement, and ice accretion. As a primary example, the effects of roughness, ice density, and number of shots on aerodynamic performance degradation were investigated through sensitivity analysis. The degradation of the lift coefficient (ΔC_L) is defined as the difference between the lift coefficient of clean and iced airfoils.

The sensitivity indices of roughness, ice density, and number of shots on lift degradation are shown in Fig. 22 (left). In the first-order effect, the roughness contributes to lift degradation more than ice density and number of shots. Despite the interaction effect of ice density, the total effect of roughness is much higher than that of ice density and number of shots.

The same phenomenon is illustrated by the contour map of lift degradation shown in Fig. 22 (right). The lift degradation is very insignificant at low roughness and increases with increasing roughness. At low roughness, the reduced convective cooling due to lower heat flux reduces the ice accretion and excludes the horn-shaped glaze ice accretion, which in turn leads to negligible lift degradation. This feature does not change very much regarding varying ice density, indicating the insignificance of ice

38

density. Further, the effect of the number of shots effect can be easily observed in Fig. 22 (right). The lift degradation increases with increasing number of shots. Higher number of shots (12 maximum number of shots) increases the number of updated air flow field and droplet solutions in the ice accretion simulation, which significantly affects the shape of ice horns. It can be seen from Figs. 18 and 19 that the number of shots has significant effect in determining the height and angle of ice horn, which can in turn affect the lift on an airfoil.
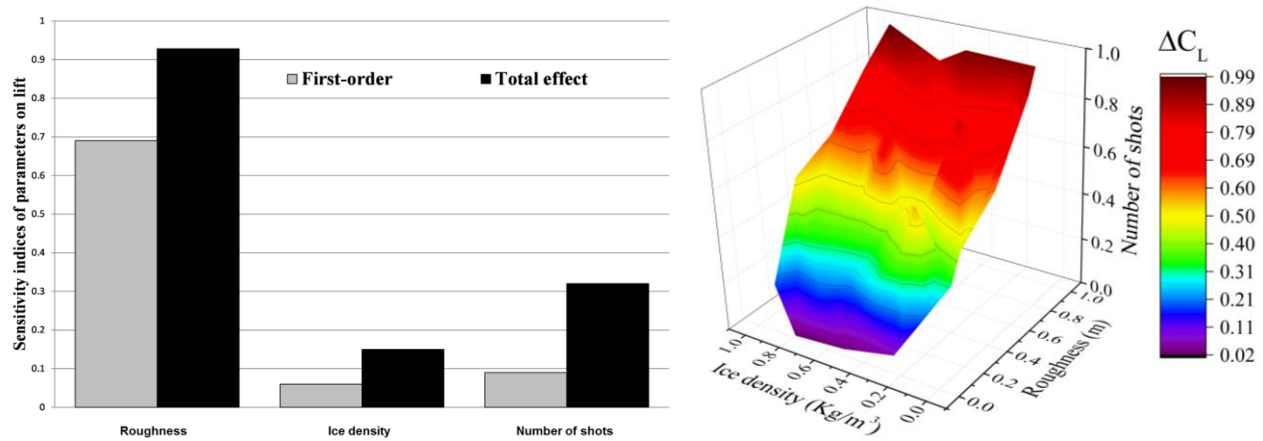

Fig. 22. Sensitivity indices (left) and contour map (right) of roughness, ice density, and number of shots on lift degradation.
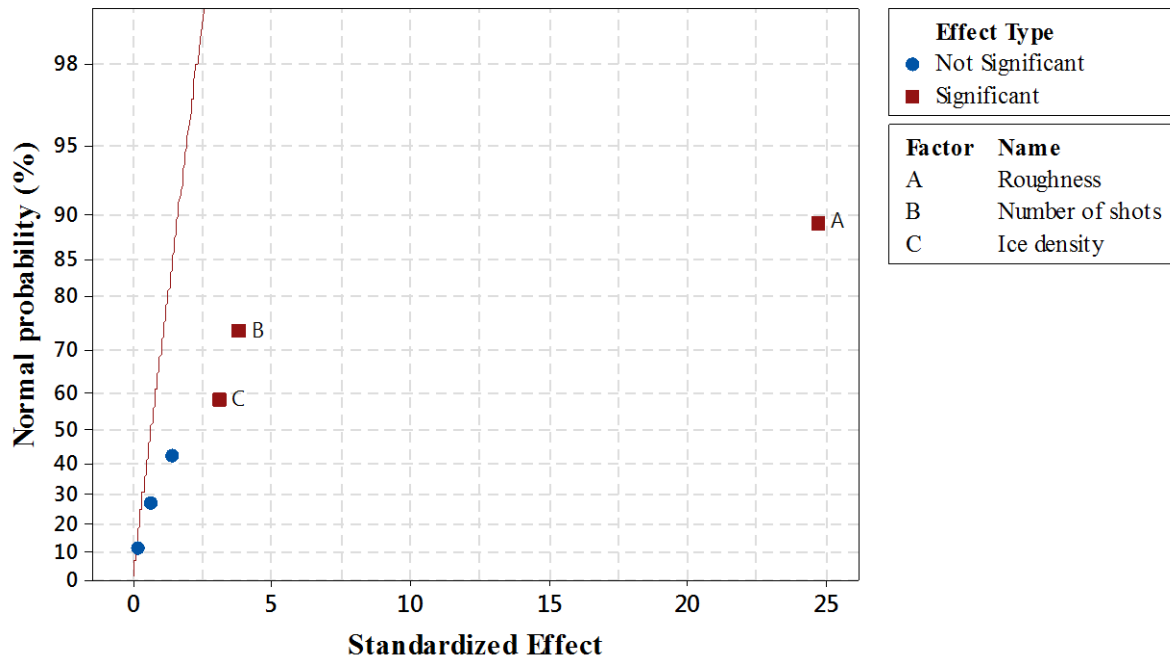
Fig. 23. Significance of roughness, ice density, and number of shots on lift degradation.

The plot of the effects also illustrates the same result, as shown in Fig. 23. The effect of roughness on lift degradation is more significant than the ice density and number of shots. In fact, from Fig. 14 (left), it was shown that the roughness significantly affected the ice horn angle and ice horn position; in particular, on the upper surface of an airfoil. It is well known from previous studies that the angle and position of the ice horn have a strong effect on lift degradation. The present analysis confirms such findings, using the first-order and total sensitivity indices and the normal probability plot of the effects.

A summary of physical explanations of effects of critical physical and modeling parameters on ice accretion and lift degradation is given in Table 3.

Table 3 Physical explanations of effects of critical physical and modeling parameters and recommendations

Effects of critical parameters	Physical explanations based on the current sensitivity analysis and recommendations

Complicated effect of roughness on ice accretion and lift degradation	Surface roughness affects ice horn height and ice horn position through the strong connection between roughness and heat flux. An increase in roughness significantly increases the heat transfer coefficients, which in turn increases the convective cooling and accretion of ice. Roughness also significantly affects ice horn angle and ice horn position; in particular, on the upper surface of an airfoil, which leads to severe lift degradation. Thus, a proper roughness model is necessary to accurately predict position, height, and angle of ice horn, and lift degradation.
Effect of ice density on ice shape attributes and mass	Ice density significantly affects ice mass and ice horn height on the upper surface of an airfoil. The mass of ice changes substantially together with the ice horn height, if ice density varies with given icing conditions.
Interaction effect of roughness and ice density on ice mass	In addition to ice density, the interaction effect of surface roughness and ice density was found to significantly contribute to ice mass. Ice ingestion is the main concern in the certification of engine air intakes of rotorcraft. Along with the ice density model, a roughness model is thus essential to accurately predict ice mass.
Effect of the number of shots on ice accretion	In multi-shot simulations, the air flow field and droplet solutions are updated after a certain number of ice accretion time steps, producing more realistic ice shape than the single shot simulation. The number of shots appeared in multiple interactions far more than as a single entity. The total sensitivity indices of the number of shots on ice mass significantly increases. A possible explanation for this property may be that the number of shots affects all ice accretion processes through the multiple updates of the air flow field, droplet solution, and ice shape.
Ice accretion limit and design of ice protection systems	In general, the poly-dispersed droplet distribution broadens the impingement limits; in particular, at the upper surface of the airfoil, since droplets in the low and high end of the droplet distribution tend to bring more diverse impingement patterns. This broadening may have an

	important implication in designing effective ice protection systems.
Interaction effect of droplet distribution and evaporation model	The interaction effect of droplet distribution and evaporation model is significant in determining position and angle of ice horn. This interaction has a significant effect on the ice accretion limit on the upper surface of an airfoil.

5. Conclusions and remarks

High-fidelity PDE-based aerodynamic, icing, and thermal simulations are increasingly being used to produce artificial ice shapes for certification, for determining degradation in aerodynamic performance, and designing the ice protection systems for the safe flight of aircraft in icing conditions. Further, they are used, in direct and indirect ways, to assist in icing tunnel testing and flight-testing campaigns.

However, even as these simulation methods are being more frequently applied to real world problems, questions regarding the accuracy and criticality of several physical and modeling parameters essential to these simulation methods have been raised. In order to tackle this problem, the sensitivity of critical physical and modeling parameters—four physical (surface roughness, ice density, droplet distribution, evaporation) and one modeling (single shot or multi-shot)—on eight ice shape attributes and ice mass. The effects of primary physical (surface roughness and ice density) and modeling (multi-shot) parameters on aerodynamic performance degradation of an iced airfoil were also investigated. In the analysis of clean air, droplet impingement, ice accretion, and aerodynamic performance degradation, in-house unified computational solvers based on an unstructured upwind finite volume formulation were used. In the sensitivity analysis, the Sobol sequence sampling method, the RBF, and the Sobol's method were used to generate the sampling points in the given design space, construct the metamodel, and evaluate the sensitivity indices, respectively.

According to the sensitivity indices, surface roughness was determined to be the dominant parameter affecting ice horn height and ice horn position, through the strong connection between roughness and heat

flux. Moreover, increased surface roughness leads to severe lift degradation by significantly affecting the ice horn angle and ice horn position; in particular, on the upper surface of an airfoil.

The number of shots, another important parameter, was shown to be the largest contributor in the sum of both the first-order and total effects. Also, the number of shots was found to have higher interaction effects than the main effects. This was confirmed because it appeared in multiple interactions far more than as a single entity. All these results indicate the extreme importance of the number of shots in the ice accretion simulation.

The sensitivity analysis also showed that ice density significantly affects ice mass and ice horn height on the upper surface of an airfoil, if the ice density varies with given icing conditions. This may have important implications for the design of mass-sensitive ice protection systems like the engine air intakes of rotorcraft.

Surprisingly, the evaporation model did not have a significant direct effect on any of the ice shape attributes. However, the effect of interaction between the evaporation model and droplet distribution was found to be significant in determining the ice horn position and angle, and the ice accretion limit on the upper surface of an airfoil.

In summary, it was shown that each parameter has a direct effect to a varying degree on ice accretion attributes and aerodynamic degradation. It was also noted that the interaction of parameters has a significant effect on the ice accretion attributes. This includes, for example, evaporation—droplet distribution, and roughness—number of shots—evaporation interactions. Hence, the selection of proper physical models and simulation methods can help accurately predict ice accretion and aerodynamic performance degradation.

More accurate modeling of the surface roughness requires further investigation. This may require, for example, considering the microscopic effects and chord-wise variations of ice roughness in the model. Moreover, the physical parameters involved in the ice accretion of supercooled large droplet (SLD) need to be studied. Further study on the effects of some of the parameter combinations on the ice accretion and

associated physical mechanisms is needed. We hope to report the investigation of these challenging subjects in near future.

Acknowledgments

References

[1] Landsberg B. Safety Advisor: Aircraft Icing. AOPA Air Safety Foundation; 2008.
[2] Jones SM, Reveley MS, Evans JK, Barrientos FA. Subsonic aircraft safety icing study. 2008.
[3] AI-Khalil KM. Ice accretion and performance degradation calculations with LEWICE/NS. 31st Aerospace Sciences Meeting and Exhibit: American Institute of Aeronautics and Astronautics; 1993.
[4] Wright WB. Validation Results for LEWICE 3.0. NASA Glenn Research Center; 2005.
[5] Nakakita K, Nadarajah S, Habashi W. Toward real-time aero-icing simulation of complete aircraft via FENSAP-ICE. Journal of Aircraft. 2010;47:96.
[6] Bourgault Y, Boutanios Z, Habashi WG. Three-dimensional Eulerian approach to droplet impingement simulation using FENSAP-ICE, Part 1: Model, algorithm, and validation. Journal of Aircraft. 2000;37:95-103.
[7] Lozowski E, Stallabrass J, Hearty P. The icing of an unheated, nonrotating cylinder. Part II. Icing wind tunnel experiments. Journal of Climate and Applied Meteorology. 1983;22:2063-74.
[8] Fortin G, Perron J. Spinning rotor blade tests in icing wind tunnel. 1st AIAA Atmospheric and Space Environments Conference: American Institute of Aeronautics and Astronautics; 2009.
[9] Mayer C, Ilinca A, Fortin G, Perron J. Wind tunnel study of electro-thermal de-icing of wind turbine blades. International Journal of Offshore and Polar Engineering. 2007;17.
[10] Papadakis M, Yeong H-W, Wong S-C, Vargas M, Potapczuk M. Experimental investigation of ice accretion effects on a swept wing. NASA Glenn Research Center; 2005.
[11] Papadakis M, Hung KE, Vu GT, Yeong HW, Bidwell CS, Breer MD, Bencic, TJ. Experimental investigation of water droplet impingement on airfoils, finite wings, and an S-duct engine inlet. NASA Glenn Research Center; 2002.
[12] Ratvasky TP, Van Zante JF, Sim A. NASA/FAA tailplane icing program: flight test report. NASA Lewis Research Center; 2000.
[13] Shaw R, Richter G. The UH-1H helicopter icing flight test program-An overview. 23rd Aerospace Sciences Meeting: American Institute of Aeronautics and Astronautics; 1985.
[14] Isaac G, Cober S, Strapp J, Korolev A, Tremblay A, Marcotte D. Recent Canadian research on aircraft in-flight icing. Canadian Aeronautics and Space Journal. 2001;47:213-21.
[15] Ahn GB, Jung KY, Myong RS, Shin HB, Habashi WG. Numerical and experimental investigation of ice accretion on rotorcraft engine air intake. Journal of Aircraft. 2015;52:903-9.
[16] Cao Y, Tan W, Wu Z. Aircraft icing: An ongoing threat to aviation safety. Aerospace Science and Technology. 2018;75:353-85.
[17] Jin W. Numerical investigation of icing effects on dynamic inlet distortion. International Journal of Aeronautical and Space Sciences. 2018;19:354-62.
[18] Cao Y, Ma C, Zhang Q, Sheridan J. Numerical simulation of ice accretions on an aircraft wing. Aerospace Science and Technology. 2012;23:296-304.
[19] MyersĪ TG. Extension to the Messinger model for aircraft icing. AIAA Journal. 2001;39.
[20] Raj LP, Lee JW, Myong RS. Ice accretion and aerodynamic effects on a multi-element airfoil under SLD icing conditions. Aerospace Science and Technology. 2018;85:320-33.

[21] Budinger M, Pommier-Budinger V, Bennani L, Rouset P, Bonaccurso E, Dezitter F. Electromechanical resonant ice protection systems: analysis of fracture propagation mechanisms. AIAA Journal. 2018;56:4412-22.

[22] Overmeyer A, Palacios J, Smith E. Ultrasonic de-icing bondline design and rotor ice testing. AIAA Journal. 2013;51:2965-76.

[23] Mirzaei M, Ardekani MA, Doosttalab M. Numerical and experimental study of flow field characteristics of an iced airfoil. Aerospace Science and Technology. 2009;13:267-76.

[24] Han Y, Palacios J. Airfoil-performance-degradation prediction based on nondimensional icing parameters. AIAA Journal. 2013;51:2570-81.

[25] Miller D, Potapczuk M, Langhals T. Preliminary investigation of ice shape sensitivity to parameter variations. 43rd AIAA Aerospace Sciences Meeting and Exhibit: American Institute of Aeronautics and Astronautics; 2005.

[26] Beaugendre H, Morency F, Habashi WG. FENSAP-ICE's three-dimensional in-flight ice accretion module: ICE3D. Journal of Aircraft. 2003;40:239-47.

[27] Gent RW, Dart NP, Cansdale JT. Aircraft icing. Philosophical Transactions of the Royal Society of London A: Mathematical, Physical and Engineering Sciences. 2000;358:2873-911.

[28] Han Y, Palacios J. Surface roughness and heat transfer improved predictions for aircraft ice-accretion modeling. AIAA Journal. 2017:1318-31.

[29] Ruff GA, Berkowitz BM. Users manual for the NASA Lewis ice accretion prediction code (LEWICE). NASA CR-185129: NASA Glenn Research Center; 1990.

[30] Shin J, Bond TH. Experimental and computational ice shapes and resulting drag increase for a NACA 0012 airfoil. National Aeronautics and Space Administration; 1992.

[31] Macklin W. The density and structure of ice formed by accretion. Quarterly Journal of the Royal Meteorological Society. 1962;88:30-50.

[32] Jones KF. The density of natural ice accretions related to nondimensional icing parameters. Quarterly Journal of the Royal Meteorological Society. 1990;116:477-96.

[33] Campbell SE, Broeren AP, Bragg MB. Sensitivity of aircraft performance to icing parameter variations. Journal of Aircraft. 2007;44:1758-60.

[34] Wright WB. Validation Process for LEWICE by Use of a Naviér-Stokes Solver. 8th AIAA Atmospheric and Space Environments Conference: American Institute of Aeronautics and Astronautics; 2016.

[35] Wright WB. A revised validation process for ice accretion codes. 9th AIAA Atmospheric and Space Environments Conference: American Institute of Aeronautics and Astronautics; 2017.

[36] Son C, Oh S, Yee K. Quantitative analysis of a two-dimensional ice accretion on airfoils. Journal of Mechanical Science and Technology. 2012;26:1059-71.

[37] Son C, Oh S, Yee K. Quantitative investigation into the relationship between ice accretion shape and ambient conditions. Transactions of the Japan Society for Aeronautical and Space Sciences. 2013;56:175-86.

[38] DeGennaro A, Rowley CW, Martinelli L. Data-driven low-dimensional modeling and uncertainty quantification for airfoil icing. 33rd AIAA Applied Aerodynamics Conference: American Institute of Aeronautics and Astronautics; 2015.

[39] Lampton A, Valasek J. Prediction of icing effects on the lateral/directional stability and control of light airplanes. Aerospace Science and Technology. 2012;23:305-11.

[40] Marongiu C, Vitagliano P, Zanazzi G, Narducci R. Aerodynamic analysis of an iced airfoil at medium/high reynolds number. AIAA Journal. 2008;46:2469-78.

[41] Chen X, Zhao Q, Barakos G. Numerical analysis of aerodynamic characteristics of iced rotor in forward flight. AIAA Journal. 2018:1-15.

[42] Jung SK, Myong RS. A second-order positivity-preserving finite volume upwind scheme for air-mixed droplet flow in atmospheric icing. Computers & Fluids. 2013;86:459-69.

[43] Lapple C. Fluid and Particle Mechanics: Vincent Press; 2007.

[44] Morency F, Tezok F, Paraschivoiu I. Anti-icing system simulation using CANICE. Journal of Aircraft. 1999;36:999-1006.

[45] Bourgault Y, Beaugendre H, Habashi W. Development of a shallow-water icing model in FENSAP-ICE. Journal of Aircraft. 2000;37:640-6.

[46] Roe PL. Approximate Riemann solvers, parameter vectors, and difference schemes. Journal of Computational Physics. 1981;43:357-72.

[47] Blazek J. Computational Fluid Dynamics: Principles and Applications: Elsevier; 2005.

[48] Swanson R, Turkel E. A multistage time-stepping scheme for the Navier-Stokes equations. 23rd Aerospace Sciences Meeting: American Institute of Aeronautics and Astronautics; 1985.

[49] Homma T, Saltelli A. Importance measures in global sensitivity analysis of nonlinear models. Reliability Engineering & System Safety. 1996;52:1-17.

[50] Sobol IM. Global sensitivity indices for nonlinear mathematical models and their Monte Carlo estimates. Mathematics and Computers in Simulation. 2001;55:271-80.

[51] Chen W, Jin R, Sudjianto A. Analytical variance-based global sensitivity analysis in simulation-based design under uncertainty. Journal of Mechanical Design. 2005;127:875-86.

[52] Werbos PJ. Applications of advances in nonlinear sensitivity analysis. System Modeling and Optimization: Springer; 1982. p. 762-70.

[53] Sudret B. Global sensitivity analysis using polynomial chaos expansions. Reliability Engineering & System Safety. 2008;93:964-79.

[54] Saltelli A. Making best use of model evaluations to compute sensitivity indices. Computer Physics Communications. 2002;145:280-97.

[55] Martin JD, Simpson TW. Use of kriging models to approximate deterministic computer models. AIAA Journal. 2005;43:853-63.

[56] Oakley JE, O'Hagan A. Probabilistic sensitivity analysis of complex models: a Bayesian approach. Journal of the Royal Statistical Society: Series B (Statistical Methodology). 2004;66:751-69.

[57] Mullur AA, Messac A. Extended radial basis functions: more flexible and effective metamodeling. AIAA Journal. 2005;43:1306-15.

[58] Burhenne S, Tsvetkova O, Jacob D, Henze GP, Wagner A. Uncertainty quantification for combined building performance and cost-benefit analyses. Building and Environment. 2013;62:143-54.

[59] Hardy RL. Multiquadric equations of topography and other irregular surfaces. Journal of Geophysical Research. 1971;76:1905-15.

[60] Chilton TH, Colburn AP. Mass transfer (absorption) coefficients prediction from data on heat transfer and fluid friction. Industrial & Engineering Chemistry. 1934;26:1183-7.

[61] Kim H, Bragg M. Effects of leading-edge ice accretion geometry on airfoil performance. 17th Applied Aerodynamics Conference: American Institute of Aeronautics and Astronautics; 1999.